

Optically thin circumstellar medium in β Lyr A system

M. Brož¹, D. Mourard², J. Budaj³, P. Harmanec¹, H. Schmitt⁴, I. Tallon-Bosc⁵, D. Bonneau², H. Božić⁶, D. Gies⁷, and M. Šlechta⁸

¹ Astronomical Institute of the Charles University, Faculty of Mathematics and Physics,
V Holešovičkách 2, 180 00 Praha 8, Czech Republic

² Université Côte d'Azur, OCA, CNRS, Lagrange, Parc Valrose, Bât. Fizeau, 06108 Nice, France

³ Astronomical Institute, Slovak Academy of Sciences, 059 60 Tatranská Lomnica, Slovak Republic

⁴ Naval Research Laboratory, Remote Sensing Division, Code 7215, 4555 Overlook Ave. SW, Washington, DC 20375, USA

⁵ Univ Lyon, Univ Lyon1, Ens de Lyon, CNRS, Centre de Recherche Astrophysique de Lyon UMR5574, F-69230, Saint-Genis-Laval, France

⁶ Hvar Observatory, Faculty of Geodesy, University of Zagreb, Kačićeva 26, 10000 Zagreb, Croatia

⁷ The CHARA Array of Georgia State University, Mount Wilson Observatory, Mount Wilson, California 91023, USA

⁸ Astronomical Institute, Czech Academy of Sciences, 251 65 Ondřejov, Czech Republic

Received October 13, 2020

ABSTRACT

β Lyr A is a complex binary system with an extensive observational dataset: light curves (from FUV to FIR), interferometric squared visibility, closure phase, triple product measurements, spectral-energy distribution (SED), high-resolution spectroscopy, differential visibility amplitude, and also differential phase. In particular, we use spectra from Ondřejov 2m telescope from 2013 to 2015, to measure the emission in H α , He I, Si II, Ne I, or C II lines, and differential interferometry by CHARA/VEGA from the 2013 campaign to measure wavelength-dependent sizes across H α and He I 6678. This allows us to constrain not only optically thick objects (primary, secondary, accretion disk), but also optically thin objects (disk atmosphere, jets, shell). We extended our modelling tool Pshellspec (based on Shellspec; a 1D LTE radiative transfer code) to include all new observables, to compute differential visibilities/phases, to perform a Doppler tomography, and to determine a joint χ^2 metric. After an optimisation of 38 free parameters, we derive a robust model of the β Lyr A system. According to the model, the emission is formed in an extended atmosphere of the disk, two perpendicular jets expanding at ~ 700 km s⁻¹, and a symmetric shell with the radius $\sim 70 R_{\odot}$. The spectroscopy indicates a low abundance of carbon, 10^{-2} of the solar value. We also quantify systematic differences between datasets and discuss alternative models, with higher resolution, additional asymmetries, or He-rich abundance.

Key words. Stars: close – Stars: binaries: spectroscopic – Stars: binaries: eclipsing – Stars: emission-line – Stars: individual: β Lyr A

1. Introduction

β Lyr A (HR 7106, HD 174638) is an archetype of a semidetached binary in a rather rapid phase of mass transfer (of the order of $2 \cdot 10^{-5} M_{\odot} \text{ yr}^{-1}$) between binary components. Its orbital period has been increasing by the high rate of 19 sec per year. While during the interferometric campaign in 2013 the value of the period was 12^d9427, in 2020 it is already 12^d9440. The gainer (primary) is an early B star hidden in an optically thick accretion disk. The donor (secondary) is a late B star filling its Roche lobe. For a summary of numerous investigations of this object, we refer the readers to Sahade (1966), Harmanec (2002), Skulskii (2020).

In Mourard et al. (2018), we summarized more recent studies and carried out an attempt to model optically thick matter within the system. The model of β Lyr A was constrained by wide-band light curves (FUV to FIR) and continuum interferometric measurements. It was thus sensitive to the properties of the Roche-filling secondary, the primary and its opaque accretion disk. The following values were adopted from the previous studies: semi-amplitudes of the radial-velocity (RV) curves $K_1 = 41.4$ km s⁻¹, $K_2 = 186.3$ km s⁻¹, implying the inverse mass ratio $q = 0.223$, the projected semimajor axis $a \sin i = 58.19 R_{\odot}$ and the masses

$M_2 = 13.048 M_{\odot}$, $M_1 = 2.910 M_{\odot}$. The model led to an estimated distance to the system of ~ 320 pc and to the finding that the accretion disk fills the whole available space of the Roche lobe in the orbital plane.

This study represents an extension of that work to optically thin parts of circumstellar matter within the system. To this goal, we shall use additional observational data, in particular spectral-energy distribution (SED), high-resolution spectroscopy, and differential interferometry to measure absolute fluxes, emission line profiles, wavelength-dependent brightness distribution at the same time. This allows us to model the properties of the disk atmosphere, jets, or possible shell-like structures. To this point, we use a *geometrically constrained* model, described by a limited set of geometrical objects and a limited number of parameters. This method has been preferred because an image reconstruction from limited spatial frequencies of interferometric measurements was not possible. On the other hand, any geometrical model uses numerous assumptions, e.g., the Roche geometry for stellar surfaces, some symmetries, or an a-priori knowledge.

2. Observational data

All observational data used in our previous study (Mourard et al. 2018) remain the same, i.e., the light curves and optical interfero-

Send offprint requests to: e-mail: mira@sirrah.troja.mff.cuni.cz

metric data. We thus refer to this work for their detailed description. We just recall that the interferometric measurements give access to information on the brightness spatial distribution of the source. The squared visibilities sample the Fourier transform of the distribution at a spatial frequency defined by the baseline vector projected on the plane of sky divided by the central wavelength of the observed band, \mathbf{B}/λ . Closure phase and triple product amplitudes are self-calibrated estimators based on the interferometric data considered on a triplet of telescopes. Hereinafter, we describe only the additionally used data.

2.1. Spectral-energy distribution (SED)

To constrain the absolute flux of β Lyr A, we use data from Burnashev & Skulskii (1978). This low-resolution absolute spectrophotometry covers the wavelength range from 3300 to 7400 Å, i.e., including the $H\alpha$, $H\beta$, $H\gamma$, $H\delta$, the Balmer jump, as well as the He I 5876 and 6678 lines. The effective bands are 25 Å wide which is not enough to resolve the spectral lines. These are well represented by our high-resolution spectra described below. The fluxes were calibrated on Vega (α Lyr), based on its absolute calibration by Tereshchenko & Kharitonov (1972). When interpreting these fluxes, one should be more careful in the NUV region, where the calibration is generally more difficult.

We performed a dereddening of the absolute fluxes to account for interstellar extinction. For the galactic coordinates $l = 63.1876^\circ$, $b = 14.7835^\circ$ and the distance moduli $\mu = 5 \log_{10}[d]_{\text{pc}} - 5 \doteq 7.3$ to 7.6 we would expect a value at most $E(B - V) = 0.020$ (Green et al. 2015). Using standard relations for $A_V = 3.1 E(B - V)$ and A_λ/A_V (Schlafly & Finkbeiner 2011), we increased the observed absolute fluxes F_λ accordingly.

2.2. High-resolution spectroscopy (SPE)

We have at our disposal 72 Ondřejov CCD spectra from 2013 to 2015 (JDs 2456450.37 to 2457294.30). The spectra have a linear dispersion of 17.2 \AA mm^{-1} and a two-pixel resolution of 12700. They cover the wavelength region of approximately 6300 to 6730 Å. Their initial reductions (flatfielding, wavelength calibrations and creation of 1-D spectra) were carried out by MŠ in IRAF. Normalization and measurement of a selection of telluric lines to be used for a fine correction of radial-velocity (RV) zero point were carried out by PH in SPEFO (Horn et al. 1996; Krpata 2008). For modelling, we used a selection of 11 spectra, well covering different phases of the orbital period.

Given the nature of the β Lyr A system, we shall perform a Doppler-tomography analysis. This should enable us to resolve a 3-D structure and velocity fields of the circumstellar matter.

2.3. Differential interferometry (VAMP, VPHI)

In Mourard et al. (2018) we have presented an extensive interferometric data set recorded during a coordinated campaign in 2013. Data were obtained on the NPOI array (Armstrong et al. 1998), and on the CHARA Array (ten Brummelaar et al. 2005) with the MIRC (Monnier et al. 2004) and VEGA (Mourard et al. 2009, 2011) instruments. This first paper was dedicated to the study of the opaque accretion disk and has made use of all the interferometric measurements in the continuum bands from 525 to 861 nm and in the H band.

For the work presented here, the VEGA data are used to measure differential complex visibilities in the $H\alpha$ (6562 Å) and He I

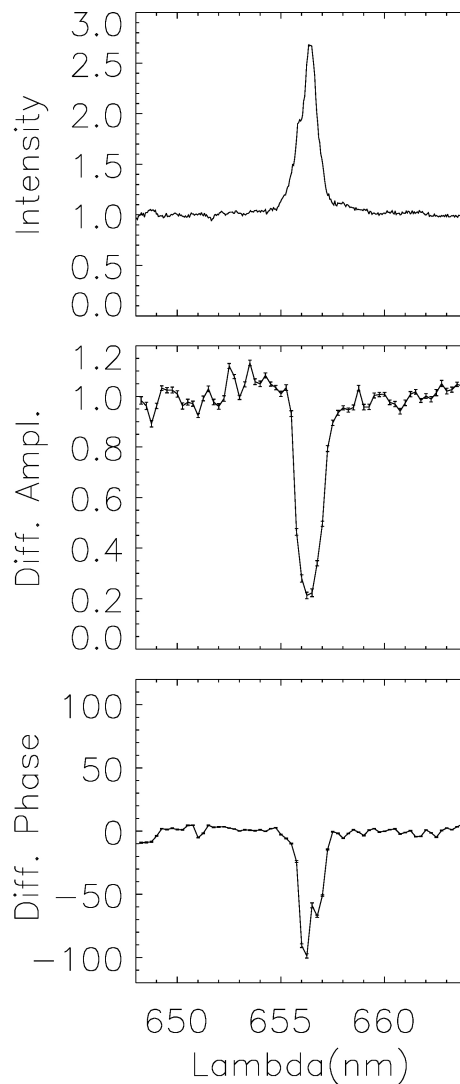


Fig. 1. An example of the VEGA differential visibility measurement during the night of 27 Jun 2013 with the 140 m E2W2 baseline. Top: the $H\alpha$ line (continuum normalized to 1); middle: Amplitude of the differential visibility (normalized to 1 in the continuum); bottom: phase of the differential visibility in degrees.

(6678 and 7065 Å) lines. Differential complex visibilities are estimated through the cross-spectrum of the interferometric data between a first wide reference spectral band and a second narrow analysis band crossing the first one. Knowing the shape of the object from the squared visibilities in the reference band, the differential data permit to extract information on the variation of the shape of the object at high spectral and spatial resolution over a small band. The amplitude gives information on the chromatic dependence of the size of the object whereas the phase provides valuable information on the position on the sky.

202 measurements (87 for $H\alpha$, 87 for He I 6678, and 28 for He I 7065) are available with both differential amplitude and phase, with a standard deviation of phase in the continuum smaller than 15° . In the case of a larger standard deviation of the differential phase, we got 498 additional measurements of the amplitude of the differential visibility (195 for $H\alpha$, 204 for He I 6678, and 99 for He I 7065) with a signal to noise ratio better than 5 in the continuum. The details of the observations are presented in Mourard et al. (2018).

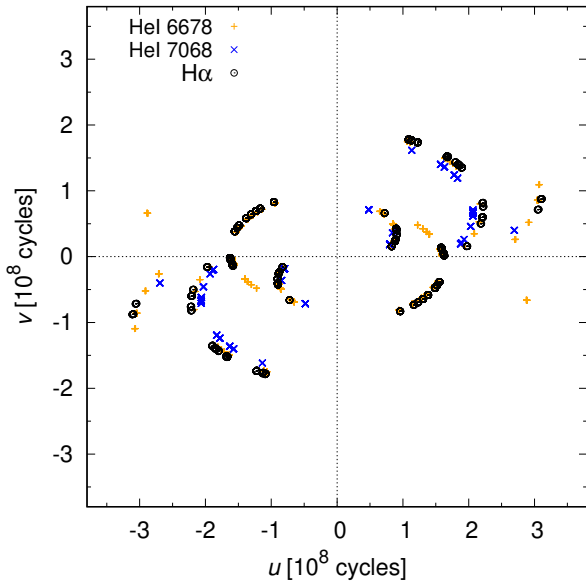


Fig. 2. The (u, v) coverage of differential visibility and phase measurements from the CHARA/VEGA instrument. A subset of H α data used for modelling is shown (black), together with additional He I 6678 (green) and 7065 (blue) data. The orientation is $v > 0$ north and $u > 0$ east.

The standard differential processing (Mourard et al. 2009) of the VEGA data has been modified to avoid the underestimation of the uncertainties of the differential quantities. For this work, we have replaced them by the standard deviation of the measurements (both amplitude and phase) computed in the continuum part and multiplied by a factor equal to the square root of the flux of each narrow-band channel in order to correctly match the behavior of the photon noise.

One example of an individual measurement is presented in Figure 1. It should be noted that the amplitude of the differential visibility is normalized to 1 in the continuum and that the phase is arbitrarily set to a mean value of 0 in the continuum. It is also important to note that, in some cases, phase jumps may occur as the differential phase is defined only modulo 2π . The (u, v) coverage is shown in Figure 2.

3. Pyshellspec model

To account for all types of observational data, we had to significantly extend and improve our modelling tool called Pyshellspec¹. Its purpose is to calculate radiative transfer through the volume surrounding the binary. We now use a joint χ^2 metric as follows:

$$\chi^2 = \chi_{\text{lc}}^2 + \chi_{\text{vis}}^2 + \chi_{\text{clo}}^2 + \chi_{\text{t3}}^2 + \chi_{\text{sed}}^2 + \chi_{\text{spe}}^2 + \chi_{\text{vamp}}^2 + \chi_{\text{vphi}}^2, \quad (1)$$

with individual contributions:

$$\chi_{\text{lc}}^2 = \sum_{k=1}^{N_{\text{band}}} \sum_{i=1}^{N_{\text{lc}k}} \left(\frac{m_{ki}^{\text{obs}} - m_{ki}^{\text{syn}}}{\sigma_{ki}} \right)^2, \quad (2)$$

$$\chi_{\text{vis}}^2 = \sum_{i=1}^{N_{\text{vis}}} \left(\frac{|V_i^{\text{obs}}|^2 - |V_i^{\text{syn}}|^2}{\sigma_i} \right)^2, \quad (3)$$

¹ <http://sirrah.troja.mff.cuni.cz/~mira/betalyr/>

$$\chi_{\text{clo}}^2 = \sum_{i=1}^{N_{\text{clo}}} \left(\frac{\arg T_{3i}^{\text{obs}} - \arg T_{3i}^{\text{syn}}}{\sigma_i} \right)^2, \quad (4)$$

$$\chi_{\text{t3}}^2 = \sum_{i=1}^{N_{\text{t3}}} \left(\frac{|T_{3i}|^{\text{obs}} - |T_{3i}|^{\text{syn}}}{\sigma_i} \right)^2, \quad (5)$$

$$\chi_{\text{sed}}^2 = \sum_{i=1}^{N_{\text{sed}}} \left(\frac{F_{\lambda i}^{\text{obs}} - F_{\lambda i}^{\text{syn}}}{\sigma_i} \right)^2, \quad (6)$$

$$\chi_{\text{spe}}^2 = \sum_{i=1}^{N_{\text{spe}}} \left(\frac{I_{\lambda i}^{\text{obs}} - I_{\lambda i}^{\text{syn}}}{\sigma_i} \right)^2, \quad (7)$$

$$\chi_{\text{vamp}}^2 = \sum_{k=1}^{N_{\text{set}}} \sum_{i=1}^{N_{\text{vamp}k}} \left(\frac{V_i^{\text{obs}} - V_i^{\text{syn}} f_k}{\sigma_i} \right)^2, \quad (8)$$

$$\chi_{\text{vphi}}^2 = \sum_{k=1}^{N_{\text{set}}} \sum_{i=1}^{N_{\text{vphi}k}} \left(\frac{\arg V_i^{\text{obs}} - \arg V_i^{\text{syn}} + g_k + h_k}{\sigma_i} \right)^2, \quad (9)$$

where m denotes magnitudes in given passbands, $|V|^2$ squared visibility, $\arg T_3$ closure phase, $|T_3|$ triple product amplitude, F_{λ} absolute monochromatic flux, I_{λ} normalized monochromatic flux, $|V|$ differential visibility amplitude, $\arg V$ differential visibility phase. The latter two interferometric quantities are modified by a multiplicative factor f_k , an additive offset g_k , and a phase slip h_k ($\pm 360^\circ$) to correctly match the way these quantities are estimated as explained in Sec. 2.3.

Apart from new observables, more objects (jet, flow, shell) were implemented in Python, and correspondingly more free parameters. We performed some corrections necessary for the high-resolution spectroscopy, in particular velocity fields of all object are propagated to Shellspec; Phoenix absolute spectra (Husser et al. 2013), used as boundary conditions at the stellar surfaces of our 3D model, were converted from vacuum to air wavelengths and a higher resolution 0.1 \AA was used. Fitting of factors, offsets and slips per each interferometric dataset was included, to minimize the difference between observed and synthetic differential visibilities and phases. Optionally, we use the subspace-searching simplex algorithm (or subplex; Rowan 1990) for the χ^2 minimisation, which is sometimes very useful. The Openmp (threads) parallelisation is done per wavelengths (for LC, VIS, VAMP, VPHI, etc. datasets) or per phases (for SED, SPE). To model extended optically thin structures, we had to extend the grid (usually $80 \times 80 R_{\odot}$), and optionally use a lower resolution ($2 R_{\odot}$ instead of $1 R_{\odot}$). A majority of rays is in a non-empty space even with these approximations, and the task is thus computationally substantially more demanding than before. For our extensive dataset, we need 3564 synthetic images per iteration, and the number of iterations is about 10^3 to achieve a convergence.

Some improvements of the original Shellspec (Budaj & Richards 2004; Budaj et al. 2005; Budaj 2011) were also implemented in Fortran. This includes a radial velocity field in disk (added on top of the Keplerian field), simple shadowing with prescribed scale height H , which allows to switch on scattering

in the disk atmosphere, a variable step in the optical depth to prevent integration artefacts. We modified priorities of overlapping objects (jets priority is higher than nebulas, and envelopes is lower than nebulas). There is a possibility to use two embedded grids, with a lower resolution for extended structures and a higher resolution in the centre. We tested also asymmetric jets, or temperature gradients in shells.

Nevertheless, we shall recall all physical properties of our model. We assume LTE level populations, LTE ionisation equilibrium, the line profile is determined by thermal, microturbulent, natural, Stark, Van der Waals broadenings, and the Doppler shift. The continuum opacity is caused by H I bound-free, H I free-free, H⁻ bound-free, H⁻ free-free transitions, the Thomson scattering on free electrons, and the Rayleigh scattering on neutral hydrogen. The scattering processes are implemented only for optically thin environment (single scattering process), with the shadowing mentioned above. The scattering is non-isotropic and is described by the dipole phase function. We also account for the line opacity of H α , He I, Si II, Ne I, and C II. Abundances are assumed to be either solar, increased up to 3 times (0.5 dex), sub-solar (in C; Section 5.8), or He-rich (Section 5.9). We use a small grid of synthetic spectra for the stars, generated by Pyterpol (Nemravová et al. 2016) from Phoenix, BSTAR, and OSTAR grids (Husser et al. 2013; Lanz & Hubený 2007, 2003). The stars are subject to the Roche geometry, limb darkening and gravity darkening (in particular the Roche-filling donor).

On the other hand, we do *not* include optical irradiation of stars, reflection (because the hot primary is mostly hidden in the disk), Mie absorption on dust, Mie scattering, or dust thermal emission. We consider these missing opacity sources negligible, because temperatures in the system are too high for dust condensation.

As in the previous study, we use the quadratic ephemeris by Ak et al. (2007):

$$T_{\min, I}(\text{HJD}) = 2408247.968(15) + 12.913779(16) \cdot E + 3.87265(369) \times 10^{-6} \cdot E^2, \quad (10)$$

which corresponds to the primary minimum of the optical light curve and in our particular case of β Lyr A the donor (secondary) is *behind* the gainer (primary; hidden in its opaque disk). Initial conditions for further convergence generally correspond to our previous model based on the optically thick medium (Mourard et al. 2018), although this model did not produce sufficient emission in lines.

Parameter relations. For an easier interpretation of results, we review some of the parameter relations (i.e., the geometrical constraints), as they are implemented in the current version of Shellspec.

The disk (a.k.a. nebula) object is described in cylindrical coordinates (R, z) (see also Tab. 2 for basic length scales):

$$H(R) = h_{\text{cnb}} \sqrt{\frac{\gamma k_B T}{\mu m_u} \frac{1}{\Omega_k}}, \quad (11)$$

$$\Sigma(R) = \Sigma_{\text{nb}} \left(\frac{R}{R_{\text{innb}}} \right)^{\epsilon_{\text{densnb}}}, \quad (12)$$

$$\rho(R, 0) = \frac{\Sigma}{\sqrt{2\pi}H}, \quad (13)$$

$$\rho(R, z) = \rho(R, 0) \exp \left[-\min \left(\frac{z^2}{2H^2}; \frac{h_{\text{windnb}}^2}{2} \right) \right], \quad (14)$$

$$T(R, 0) = T_{\text{nb}} \left(\frac{R}{R_{\text{innb}}} \right)^{\epsilon_{\text{tempnb}}}, \quad (15)$$

$$T(R, z) = T(R, 0) \max \left(1; 1 + (t_{\text{invnb}} - 1) \frac{|z| - h_{\text{invnb}}H}{a_{\text{neb}}H - h_{\text{invnb}}H} \right), \quad (16)$$

$$v_r(R) = \mathcal{H}(|z| - h_{\text{velnb}}H) v_{\text{nb}} \left(1 - \frac{R_{\text{innb}}}{R} \right)^{\epsilon_{\text{velnb}}}, \quad (17)$$

$$v_\phi(R) = \sqrt{\frac{GM_\star}{R}}, \quad (18)$$

where H is the scale height, γ the adiabatic exponent, k_B the Boltzmann constant, μ the mean molecular weight, m_u the atomic mass unit, G the gravitational constant, $\Omega_k = v_\phi/R$ the Keplerian angular velocity, Σ surface density, ρ volumetric density, T temperature, v_r radial velocity, v_ϕ azimuthal velocity; $\mathcal{H}(x)$ denotes the Heaviside step function.

The jet has a shape of a double cone with the opening angle a_{jet} and is described in spherical coordinates (R, θ) :

$$\rho(R) = \rho_{\text{jt}} \left(\frac{R_{\text{injt}}}{R} \right)^2 \frac{v_r(R_{\text{injt}})}{v_r(R)} (1 \pm a_{\text{symjt}}), \quad (19)$$

$$T(R) = T_{\text{jt}} \left(\frac{R}{R_{\text{injt}}} \right)^{\epsilon_{\text{tempjt}}}, \quad (20)$$

$$v_r(R) = v_{\text{jt}} \left(1 - \frac{R_{\text{cjt}}}{R} \right)^{\epsilon_{\text{veljt}}}. \quad (21)$$

In our case, the base plane corresponds to the orbital plane and the cone position is determined by the radial offset R_{poljt} and the polar angle α_{jet} .

Similarly, the shell is also described in spherical coordinates:

$$\rho(R) = \rho_{\text{sh}} \left(\frac{R_{\text{insh}}}{R} \right)^2 \frac{v_r(R_{\text{insh}})}{v_r(R)}, \quad (22)$$

$$T(R) = T_{\text{sh}} \left(\frac{R}{R_{\text{insh}}} \right)^{\epsilon_{\text{tempsh}}}, \quad (23)$$

$$v_r(R) = v_{\text{sh}} \left(1 - \frac{R_{\text{csh}}}{R} \right)^{\epsilon_{\text{velsh}}}, \quad (24)$$

We assume the spherical shell is centered on the primary and encompasses also other objects. It represents circumstellar matter which escaped farther away from the binary. All remaining parameters are explained in the caption of Tab. 1.

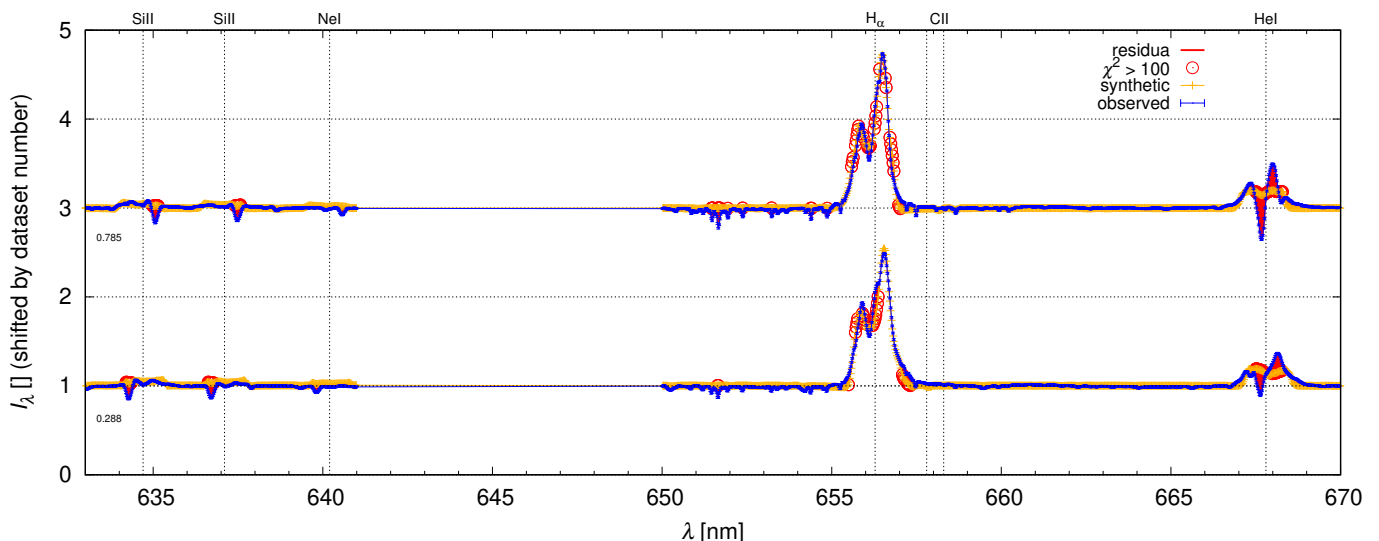


Fig. 3. Normalized spectra of β Lyr A for two out-of-eclipse phases (0.288 and 0.785). There are observed data with uncertainties indicated (blue), as well as synthetic data (yellow), residuals (red), and large χ^2 contributions (red circles). This 1st model was only fitted to these 2 spectra. The $H\alpha$ emission profile and its EW is well described, but there are systematic differences for the He I 6678 line; synthetic Si II 6347, 6371 and Ne I 6402 lines have low EW.

3.1. Doppler tomography

In order to create model spectra with enough emission, we started with two Ondřejov spectra taken at 0.288 and 0.785 phases, i.e., out of eclipses, and converged our new model with additional optically-thin objects. This simplified Doppler tomography was carried out to verify that the model is indeed capable to fit the $H\alpha$ profile. There is always a question which objects should be included in the model and which shouldn't. If the model were too simplistic, the objects would be distorted; if it were too complex, the objects could be unconstrained. After some preliminary tests we used 5 objects (primary, secondary, disk, jet, shell) out of 8 (spot, envelope, flow).²

Given the observed $H\alpha$ profiles and their overall width, our model should include a large positive velocity with respect to the line of sight, or gradient of v . Because H I, Si II, as well as He I and Ne I are excited, we expect both low and high temperatures, or gradient of T in the circumstellar medium. Apart from absorption lines arising in stellar atmospheres, the model is capable of creating a P Cygni profile due to winds, either in a disk atmosphere or in a surrounding shell. Alternatively, line profiles may be formed by overlapping velocity fields, in accord with the priorities of objects. We have to look for suitable net velocities of whole objects, but also for turbulent velocities, which significantly affect the optical depth along the line of sight; one should converge both at the same time.

Results of the first two-spectra model are shown in Figure 3. The model easily created enough emission and the EW of $H\alpha$ is fitted very well. There are relatively minor systematics in the $H\alpha$ profile, but major systematics can be seen for other spectral lines, especially He I 6678. The Si II 6347, 6371 and Ne I 6402 model lines have lower EW and depth than the observed ones, because there is a tension between the overall emission and the respective absorption. The region between 6500 and 6550 Å contains telluric lines which are *not* included in our model, but they

² A flow is presumably a relatively small structure which can overlap with a jet or a spot. An envelope is co-rotating with the binary and does not have a radially-expanding velocity field; we verified that even a Roche-filling (L2) envelope does not create enough emission. A spot is tested later as an alternative model (in Section 5.4).

should not affect the convergence in a negative way. Although we varied the chemical composition, there might be non-LTE effects (for He I) or some unaccounted temperature gradients.

A more representative set of 11 spectra covering a representative range of orbital phases was fitted in the second step. The results are shown in Figure 4. All optically-thin objects (disk atmosphere, jet, shell) contribute substantially to the $H\alpha$ emission flux. Because the spectra are normalized to the continuum flux, which is larger outside eclipses, the emission appears to vary in strength twice each orbit. The synthetic $H\alpha$ profiles for this 2nd model exhibit a variability similar to the observed ones, although at several phases there are systematic differences (both positive and negative). Comments related to He I, Si II, Ne I lines remain essentially the same.

It might seem easy to improve the fit further, but it is *not* the case for a geometrically constrained model, where all parameters have either geometrical or physical limits. We are practically sure the convergence works all right and it is not a matter of one local minimum of χ^2 . In order to improve the fit, it may be inevitable to relax some of our assumptions, e.g., the axial symmetry of the disk, the vertical symmetry of the jets, or the radial symmetry of the shell. We also do not account for any intrinsic variability of the source. However, we prefer to keep our model as simple as possible, at least at this stage.

3.2. Differential interferometry

Interestingly, all interferometric data indicate a decrease of the visibility amplitude $|dV|$ when scanning across the $H\alpha$ profile (see Figure 5) and it seems to be almost independent on baseline length and orientation (Figure 2). Such a general finding means that the core of the $H\alpha$ emitting region is clearly resolved for all baseline lengths between 50 and 200 m. Moreover, the respective velocities must be large enough to occur in the wings of $H\alpha$.

Only an extended symmetric shell may cause $|dV|$ to decrease. On contrary, a disk (nebula) or jets emit usually from small (hot) areas, and they are both asymmetric, which would force $|dV|$ to increase, at least for the shortest baselines. This is

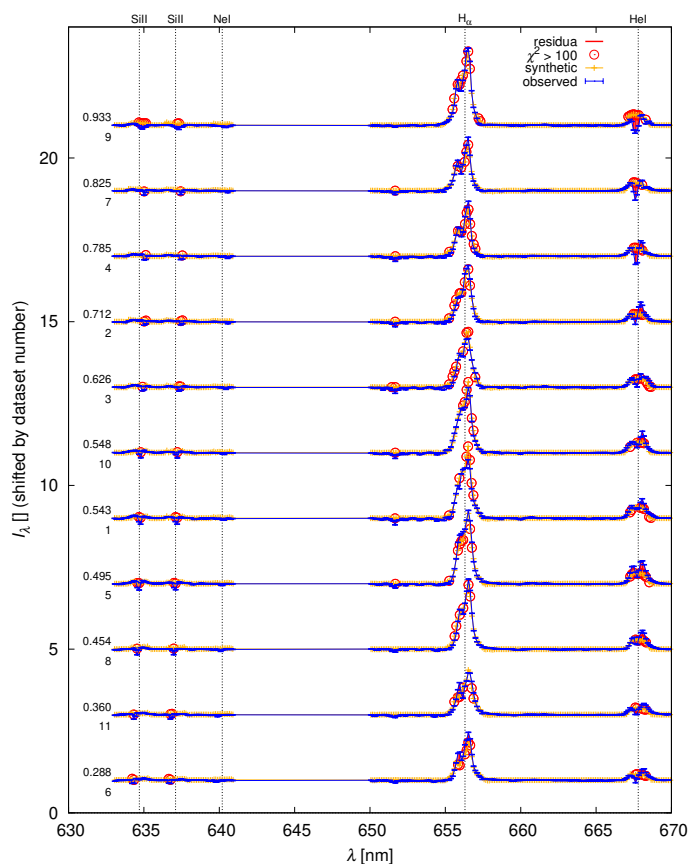


Fig. 4. Normalized spectra for 11 phases covering the whole light curve, including primary and secondary eclipses. Colours in this Fig. as well as in others have the same meaning as in Fig. 3. The synthetic $H\alpha$ profiles for the 2nd model exhibit a variability similar to the observed ones, although at several phases there are systematic differences (both + and –).

not observed. Our preliminary tests thus demonstrate the need to include the shell in our model.

Regarding the differential phase $\arg dV$ measurements, it should be noted that some phase wrappings ($\pm 360^\circ$) are present in the data (cf., e.g., datasets 1, 11, 12), which should not be a problem as we account for them in the model. The differential phases are obtained on three baselines, two of them (E1E2 and E2W2) being oriented almost perpendicular to the orbital plane, whereas the third one (W1W2) is very close in orientation to the orbital plane. Interestingly the worst fits to the model are obtained systematically for this last orientation. This general finding is in agreement with the fact that the differential phases in $H\alpha$ are dominated by the jets but we should also conclude that our geometrically-constrained model is not flexible enough to explain all the observed features.

3.3. A joint ‘compromise’ model

Our complete dataset is very heterogeneous. On one hand, this is an advantage which allows us to construct a very robust model of β Lyr A when everything is fitted together. On the other hand, when some types of measurements exhibit systematics, as mentioned above, the χ^2 contributions of the joint model will be worse while observation-specific models would be better (see Sec. 3.4).

After 2761 iterations (Figure 6), we obtained a model with reduced $\chi_R^2 = \chi^2/N$ values which are summarized in Table 1 (1st

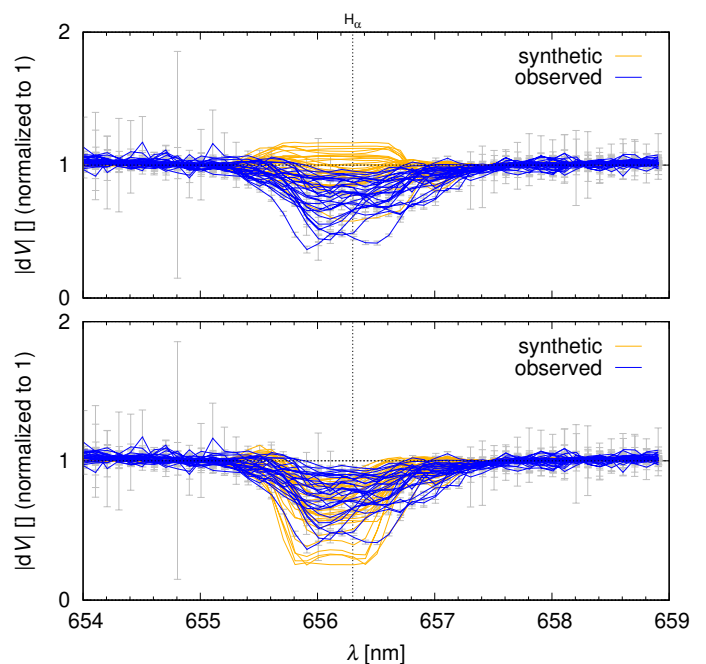


Fig. 5. Observed differential visibility amplitude $|dV|$ versus wavelength λ , normalized to 1 in the continuum (blue), and its decrease across the $H\alpha$ profile. Uncertainties of $|dV|$ are also plotted (gray). Synthetic visibilities (yellow) are shown for the two ‘extreme’ values of the shell outer radius $R_{\text{outsh}} = 40 R_\odot$ (top) and $120 R_\odot$ (bottom).

column). Previously used datasets are fitted only slightly worse than in Mourard et al. (2018), with $\chi_{\text{lc}}^2 = 3.1$, $\chi_{\text{vis}}^2 = 4.0$, $\chi_{\text{clo}}^2 = 3.4$, $\chi_{\text{t3}}^2 = 5.6$; the new datasets resulted in $\chi_{\text{sed}}^2 = 4.7$, $\chi_{\text{spe}}^2 = 44.1$, $\chi_{\text{vamp}}^2 = 4.5$, $\chi_{\text{vphi}}^2 = 44.0$, and the total $\chi_R^2 = 17.0$.

We have to explain why some contributions are large. For χ_{sed}^2 , there is a difference in NUV below the Balmer jump, which is caused by a relatively low number of measurements compared to other datasets and thus a low weight. Lines are not fitted, because the flux is computed at monochromatic wavelengths; we would have to use about 5 times higher wavelength resolution and perform a convolution with the instrumental profile of Burnashev & Skulskii (1978). Nevertheless, the line-to-continuum flux ratio is fully described by our SPE dataset. In case of χ_{spe}^2 , there are systematic differences at certain phases (0.288, 0.825), although others are good fits (0.454, 0.548, 0.712). A substantial contribution arises from high-temperature He I and Ne I lines and also from telluric lines which are not fitted by our model. For χ_{vamp}^2 , synthetic $|dV|$ sometimes exhibit a narrower decrease (cf. dataset 1), or a peak in the middle of $H\alpha$ (2, 3), although others are almost perfect fits (4, 5, 6, ...). Finally, χ_{vphi}^2 is substantially increased because synthetic $\arg dV$ are sometimes smoother (4, 6), there are possibly remaining phase slips (1, 11, 12), or mirroring of phases (2, 3); these numerous measurements have relatively high weight.

A visual comparison of all observed and synthetic datasets is shown in Figures 7, 8, 9, 10, 11, 12, 13, and 14. The resulting geometrical model of β Lyr A in the continuum is shown in Figure 15. In particular, we see optically-thick objects — the primary, the secondary and the disk — and partly also the jets, but not the tenuous shell. The same model for the wavelength range of $H\alpha$ is shown in Figure 16. We can clearly see optically-thin circumstellar matter emitting in $H\alpha$, including the velocity field. In the following we describe individual components of our model, as inferred from the observations:

PRIMARY – the gainer is an object, for which we fixed several parameters (Table 2). It is mostly hidden in the disk, but as one can see in the figures its polar region is visible. It is the source of hot radiation which is also scattered by the circumstellar medium (CSM) towards the observer.

SECONDARY – the donor is filling the Roche lobe with limb and gravity darkening. The limb darkening coefficient is interpolated for given λ from van Hamme (1993) tables. The gravity darkening parameter was set to a value suitable for non-convective atmospheres of stars (0.25). One can see that the regions near the L1 point are indeed dimmer because of it. Its polar temperature is ~ 14000 K and inferred polar radius about $14.1 R_{\odot}$.

DISK – is an axially symmetric accretion disk centered on the gainer. It has an outer radius of $31.5 R_{\odot}$ and almost fills the Roche lobe. The density profile decreases with radius and its slope (-0.57) is slightly less steep than in some Algols, where it attains -1.0 (Budaj et al. 2005; Atwood-Stone et al. 2012). The temperature profile also decreases and its slope (-0.73) is slightly steeper than a typical profile due to irradiation (-0.5) but is in surprisingly good agreement with the theoretical temperature profile of the steady viscous accretion disks (-0.75 ; Pringle 1981). The temperature at the inner rim of the disk reaches ~ 30000 K, which is a very reasonable value, comparable with the temperature of the gainer. The temperature inversion reaches 1.5 which means that the temperature increases in the vertical direction by this factor. This is most probably caused by the irradiation of the disk atmosphere. For this reason we see that the disk is brighter on the top and bottom and dimmer in the middle. Moreover, the atmosphere scatters the radiation from the gainer.

The parameter $h_{\text{cnb}} = 3.8$ means that the vertical scale height is multiplied by this factor and is more extended than the expected equilibrium value. This may be due to non-negligible hydrodynamic flows within the disk. There is a significant radial velocity component in the surface layers ($v_{\text{nb}} = 112$ km/s) which might be due to stellar wind or radiative acceleration. The turbulence is relatively low ($v_{\text{trnb}} = 11$ km/s) which means that Keplerian and radial components describe the velocity field very well.

JET – actually, two conical jets perpendicular to the orbital plane. They do not seem to be associated with the polar regions of the gainer (cf. R_{poljt}). The ‘net’ velocity v_{poljt} assigned to the jets was treated as a free parameter and we thus have to discuss whether its value 10 km s $^{-1}$ is reasonable or not. Because the projected orbital velocities of the primary and secondary are $K_1 = 41$ km s $^{-1}$ and $K_2 = -186$ km s $^{-1}$ (at the phase 0.25), we consider it to be reasonable, although indicating that the jets may not follow Keplerian velocities at the disk rim.

The terminal (expansion) velocity v_{jt} is almost 700 km/s and the respective exponent ($e_{\text{veljt}} = 1.27$) is slightly smaller than that of the shell or disk. Turbulence is about 10 times smaller than the terminal velocity which indicates that the velocity field is fitted reasonably well. This object is optically thin in continuum so it is constrained mainly by observations in the $H\alpha$ line. Without this object the reduced χ^2_{R} would increase up to 59 which justifies its role in our model (although a re-convergence might decrease it again).

SHELL – a spherical object which extends to more than $70 R_{\odot}$. The respective net velocity is low (-5 km/s); the shell may not be exactly centered and co-moving with the primary. Its terminal velocity is very low, only 79 km/s, but it is interesting that its velocity exponent is similar to that of the disk (~ 1.9). On the other hand, turbulence is very high ($v_{\text{trbsh}} = 102$ km/s) which indicates that the velocity field is not well described by

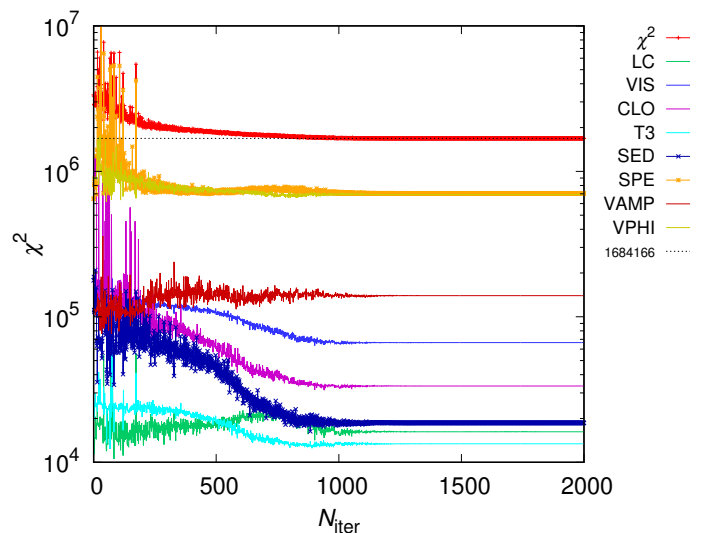


Fig. 6. The χ^2 convergence (red) for the joint model; individual contributions (LC, VIS, CLO, T3, SED, SPE, VAMP, VPHI) are also indicated. The model successfully converges to a local minimum. Some datasets have a substantially larger number of observations, i.e., effectively a larger weight. The χ^2 values are different from Tab. 1, because the model was re-converged several times and uncertainties of some datasets were modified.

our formulation (Eq. (24)). This is probably not surprising given that it fills a broad spherical region in the vicinity of the orbiting stars where gravitational potential is far from being isotropic and radial. Surprising is that our data indicate only a small radial temperature gradient (cf. e_{tmpsh}). It is also optically thin and constrained mainly by interferometry in $H\alpha$. If this object were excluded from the model the reduced χ^2_{R} would increase to 62 which also justifies its role.

Generally, the new model seems to be compatible with our previous model (Mourard et al. 2018), but we should emphasise that the major difference is the firm detection of previously conjectured structures (the jets and the shell), which was possible thanks to spectro-interferometric and spectral observations in the $H\alpha$ region. There are minor differences, however: the disk outer rim radius is larger ($R_{\text{outnb}} = 31.5$ vs previous $30 R_{\odot}$), the disk thickness slightly smaller ($h_{\text{cnb}} = 3.8$ vs 4.3), the orbital inclination also larger ($i = 96^\circ$ vs 93.5°). All these differences may be enforced by the need of emission in the $H\alpha$ line, which is enhanced if the disk is more extended and more inclined. For jets perpendicular to the disk, larger i leads to larger line-of-sight velocities and also to larger asymmetry due to the obscuration by the disk, as needed to explain the asymmetric $H\alpha$ profile. In this particular model, the asymmetries in the $H\alpha$ profile arise mostly from overlapping velocity fields of objects with increasing priorities (shell \rightarrow disk \rightarrow jet).

3.4. Observation-specific models

Starting from the ‘compromise’ model above, we converged the model again to fit individual datasets to understand the trends and potential disagreements. From the χ^2 convergence (Figure 17), it is evident that our model is indeed capable to fit individual datasets better. For example, the reduced χ^2_{ic} can easily reach 2.2 (instead of 3.1). For other χ^2 values, see Table 1 (last row). Consequently, we think there are either systematic differences between datasets, or our (complex) model is still not complete. We may miss additional objects, some asymmetries, or a

Table 1. Free parameters, χ^2 values for a joint model and for observation-specific models.

parameter	unit	joint	LC	VIS	CLO	T3	SED	SPE	VAMP	VPHI	σ
T_{cp}	K	14334	14500	14353	14591	14378	14406	14375	14592	14580	1400
R_{innb}	R_{\odot}	8.7	8.4	10.2	8.8	9.8	8.4	8.8	7.1	8.0	1.6
R_{outnb}	R_{\odot}	31.5	29.2	31.2	32.8	32.2	32.0	31.0	29.7	30.6	0.3
h_{invnb}	H	3.5	2.9	2.9	4.1	4.0	3.0	3.6	2.9	4.8	1.0
T_{invnb}	1	1.5	1.8	1.9	1.8	1.5	1.8	1.3	2.0	1.6	1.2
h_{windnb}	H	3.0	3.1	3.0	3.1	3.0	3.0	3.0	3.1	4.2	3.4
h_{cnb}	H	3.8	4.1	4.1	4.2	4.1	3.7	3.6	3.6	12.0	1.9
v_{nb}	km/s	112	112	197	114	176	96	115	199	117	40
e_{velnb}	1	1.91	1.94	1.95	1.99	1.98	1.99	1.99	2.00	1.95	0.31
h_{shdnb}	H	5.0	4.8	5.0	5.0	4.6	5.0	4.9	5.0	4.9	2.3
T_{nb}	K	30345	32260	30068	30539	32968	29662	30716	30483	33449	3300
ϱ_{nb}	10^{-9} g/cm ³	1.21	0.97	1.03	0.89	0.73	0.36	1.14	0.26	1.12	1.54
v_{trbnb}	km/s	11	42	56	13	54	98	15	93	51	17
e_{dennb}	1	-0.57	-0.77	-0.53	-0.69	-0.66	-0.52	-0.60	-0.50	-0.65	0.11
e_{tmpnb}	1	-0.73	-0.71	-0.86	-0.71	-0.71	-1.08	-0.72	-1.04	-0.72	0.07
a_{jet}	deg	28.8	23.5	47.4	29.2	32.0	30.0	28.9	33.4	26.9	7.6
R_{injt}	R_{\odot}	5.6	5.0	7.1	5.3	8.7	5.8	5.6	5.0	4.8	0.9
R_{outjt}	R_{\odot}	35.9	31.8	35.3	41.3	44.0	44.8	36.5	34.9	33.5	9.6
v_{jt}	km/s	676	1193	491	1100	1386	1405	686	876	764	~100
e_{veljt}	km/s	1.27	1.81	1.71	1.31	1.33	1.38	1.28	2.00	1.90	~0.1
T_{jt}	K	15089	16989	20274	15200	15682	15714	14712	28182	23382	1600
ϱ_{jt}	10^{-12} g/cm ³	5.52	12.54	4.24	4.83	4.61	4.14	5.41	2.52	6.39	4.21
v_{trbjt}	km/s	66	239	101	144	67	278	63	92	166	~10
R_{poljt}	R_{\odot}	33.0	32.8	32.5	34.9	33.6	33.2	32.2	34.9	34.1	4.3
v_{poljt}	km/s	10	9	18	56	71	27	12	16	60	5
α_{jt}	deg	-70	149	-34	-43	-26	-6	-71	149	-23	26
R_{insh}	R_{\odot}	7.4	7.4	8.1	9.3	7.5	17.3	7.4	7.0	7.2	1.8
R_{outsh}	R_{\odot}	72.9	62.4	60.0	86.0	76.0	100.8	73.1	84.0	67.6	25.6
v_{sh}	km/s	79	100	83	78	81	97	77	97	88	~10
e_{velsh}	1	1.90	1.38	1.80	1.77	1.86	1.06	1.88	1.96	1.94	~0.1
v_{ysh}	km/s	-5	44	-5	-23	18	-22	-9	-12	16	19
T_{sh}	K	5631	6638	5952	5705	6633	5852	5639	5562	6011	2300
ϱ_{sh}	10^{-11} g/cm ³	2.86	3.01	3.30	3.08	2.85	4.34	2.99	1.94	3.03	1.72
v_{trbsh}	km/s	102	149	111	103	109	162	100	128	109	~10
e_{tmpsh}	1	-0.01	-0.17	-0.14	-0.02	-0.05	-0.07	-0.01	-0.01	-0.06	~0.1
i	deg	96.3	96.0	95.8	96.2	96.7	96.6	96.3	96.4	96.4	0.8
Ω	deg	254.6	254.8	253.3	254.6	254.6	254.7	254.5	254.7	254.6	2.2
d	pc	328.4	327.1	322.7	329.9	327.8	328.0	328.6	329.5	329.5	7.0
N_{iter}	-	2761	1042	2561	1142	2176	1918	1798	1544	1543	
N	-	45102	2305	14354	7717	2913	1815	13338	1330	1330	
χ^2	-	767681	7083	56941	25910	16194	8578	588455	5959	58562	
χ_R^2	-	17.0	3.1	4.0	3.4	5.6	4.7	44.1	4.5	44.0	
χ^2 (spec.)	-		5176	63270	24604	21011	3866	557963	1977	31662	
χ_R^2 (spec.)	-		2.2	3.7	3.2	3.6	2.1	41.8	1.5	23.8	

Notes. T_{cp} denotes the temperature at the pole of the secondary (donor). **Disk** (a.k.a. nebula): R_{innb} inner radius, R_{outnb} outer radius, h_{invnb} inversion height, T_{invnb} temperature inversion factor, h_{windnb} wind region height, h_{cnb} scale height factor, v_{nb} terminal radial velocity, e_{velnb} its slope, h_{shdnb} shadowing height, T_{nb} temperature at the inner radius, ϱ_{nb} gas density (ditto), v_{trbnb} turbulent velocity, e_{dennb} density slope, e_{tmpnb} temperature slope. **Jet:** a_{jet} opening angle, R_{injt} inner radius, R_{outjt} outer radius, v_{jt} terminal velocity, e_{veljt} velocity slope, T_{jt} temperature, ϱ_{jt} density at the inner radius, v_{trbjt} turbulent velocity, R_{poljt} radial offset, v_{poljt} polar velocity, α_{jt} polar angle. **Shell:** R_{insh} inner radius, R_{outsh} outer radius, v_{sh} terminal velocity, e_{velsh} its slope, v_{ysh} net velocity, T_{sh} temperature, ϱ_{sh} density, v_{trbsh} turbulent velocity, e_{tmpsh} temperature slope. i is orbital inclination, Ω longitude of ascending node, and d distance.

temporal variability. Alternatively, we may modify weights of individual datasets (and use, e.g., $w_{lc} = 10$), but this does not ‘solve’ the problem, of course.

The results of all observation-specific models are summarized in Table 1 (columns ‘LC’ to ‘VPHI’). For the V band, it is also possible to compare the models visually, in Figure 18. The

differences are demonstrated as the disk thickness and the intensity of its outer edge, which is proportional to the temperature profile $T(r)$. In most models, the primary is directly visible, but the LC dataset tends to produce a continuum emission from a more extended hot area.

Table 2. Fixed parameters for the joint and observation-specific models.

parameter	unit	value
R_\star	R_\odot	5.987
T_\star	K	30000
M_\star	M_\odot	13.048
q	1	0.223
d_{gcp}	1	0.25
a_{neb}	H	5.0
h_{velnb}	H	3.0
a_{symjt}	1	0.0
$a \sin i$	R_\odot	58.19
γ	km/s	-18.0

Notes. R_\star denotes the radius of the primary (gainer), T_\star its effective temperature, M_\star mass, q mass ratio, d_{gcp} gravity darkening coefficient, a_{neb} extent of nebula, h_{velnb} minimum height for radial velocity, a_{symjt} asymmetry of jet, $a \sin i$ projected semimajor axis, and γ systemic velocity.

Given these results, uncertainties of model parameters (cf. Tab. 1; last column) were determined as the maximum differences between the joint model and *relevant* observation-specific models, because they are almost certainly dominated by systematics, not by the extent of local χ^2 minima, not even by the global one. To be more specific, σ 's for all velocities can be only constrained by the joint model and the SPE, VAMP and VPHI datasets; similarly, σ 's for flux-related quantities (ϱ , T , R) can be hardly constrained by relative measurements.

4. Stellar evolution modelling

To understand the evolutionary stage of β Lyr A binary, and its relation to the observations, we performed a simplified 1D modelling with the MESA stellar evolution program (Paxton et al. 2011, 2015). In Figure 19, we present a nominal evolution of a binary with the initial masses $M_1 = 10 M_\odot$, $M_2 = 6 M_\odot$, and the orbital period $P = 7$ d. We assumed the solar composition. We used an explicit Ritter scheme and we restricted the mass accretion rate \dot{M} up to $10^{-3} M_\odot \text{ yr}^{-1}$. Although we performed a small survey of parameters ($P = 5$ to 50 d, $M_1 = 8$ to $10 M_\odot$, while keeping $M_1 + M_2 = \text{const.}$), we restrict our discussion to the nominal case, because other values lead to binaries incompatible with β Lyr A, or to a common-envelope phase which is difficult to describe in 1D. The mass ratio q is already reversed, so that index 1 corresponds to the observed secondary (donor), and 2 to the primary (gainer).

A comparison to the observed values of a , R_1 , R_2 shows some differences: an offset 10^3 yr between the time of best-fit for a and the best-fit for M_1 , M_2 (see dotted vertical lines). The synthetic radii are a factor of 1.2 and 2 larger at this moment. However, let us recall it is only a 1D model, without an accretion disk. Consequently, we consider these differences to be acceptable. The model of van Rensbergen & De Greve (2016) produced a qualitatively similar HRD for the gainer, but their initial period was shorter, $P = 2.36$ d.

At this stage, the surface chemical composition is already modified. At $t = 19.612 \cdot 10^6$ yr, there is a low C abundance (by a factor of 10^2) and a high N abundance (by a factor of 5). At $t = 19.613 \cdot 10^6$ yr, even He abundance is increased up to 0.36 (and H correspondingly decreased). For our modelling, it means we should also test models with a substantially modified chemical composition. This is in accord with Balachandran et al.

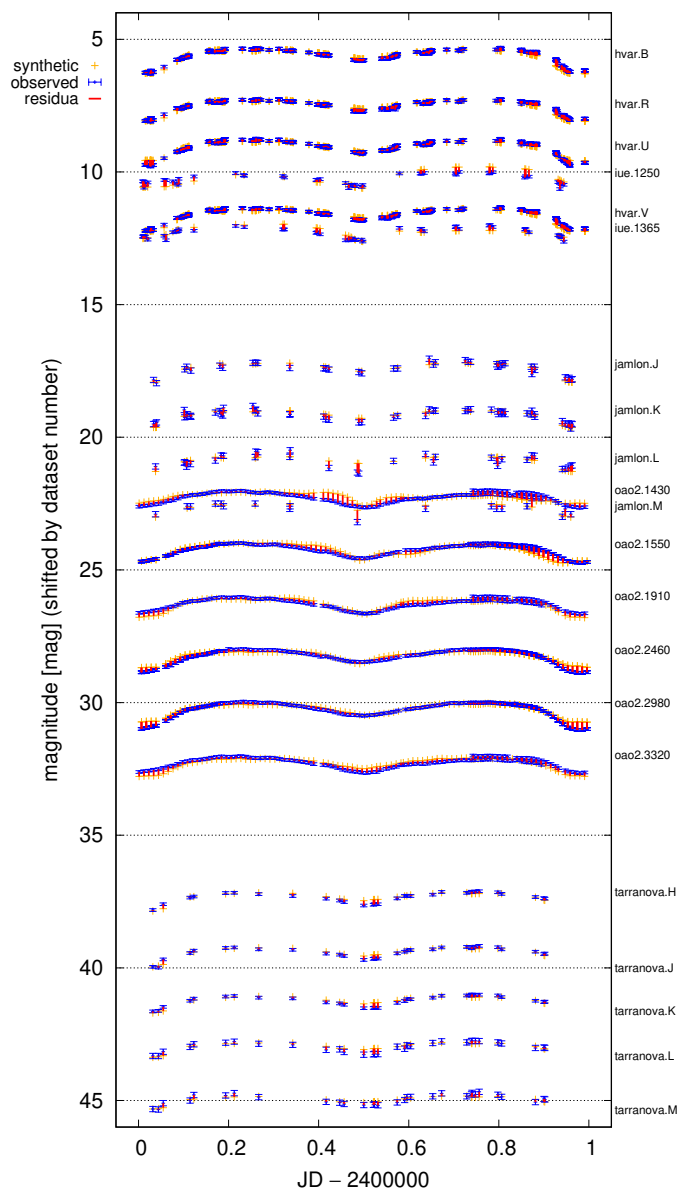


Fig. 7. Comparison of observed and synthetic phased light curves from FIR to FUV, computed for the joint ('compromise') model. The names of datasets are show in the right column. The light curves were arbitrarily shifted in the vertical direction.

(1986) who suggested He enrichment $N(\text{H}) = 0.4$, $N(\text{He}) = 0.6$ (by number), and also N to be overabundant, as well as C, O underabundant, namely $\text{C}/\text{N} \leq 0.11$, $\text{O}/\text{N} \leq 0.25$.

Interestingly, further evolution would lead to a detached system with a stripped He dwarf (secondary). A hot subdwarf of the sdB or sdO type is expected (Heber 2009; Lei et al. 2018). ϕ Per binary might be just in this (late) evolutionary stage (Mourad et al. 2015) and a dedicated comparative study might be very useful.

5. Alternative models

5.1. High-resolution model

For a spatial resolution increased twice to $1 R_\odot$, some datasets are fitted even better, e.g., χ^2_{lc} (not reduced) decreased from 7083 to 6720, because the primary and the disk rim are better re-

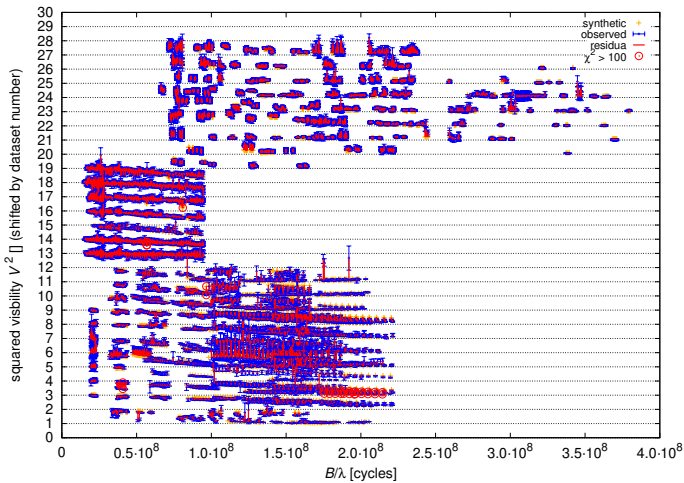


Fig. 8. Squared visibility $|V^2|$ (shifted by dataset number) for different baselines B/λ (in cycles). The are CHARA/MIRC observations at the bottom, NPOI in the middle, and CHARA/VEGA at the top (blue); synthetic data for the joint model are plotted for comparison (yellow). Overall trends ($|V^2|(B/\lambda)$) seem to be correctly described, although there are some systematics for small groups of data.

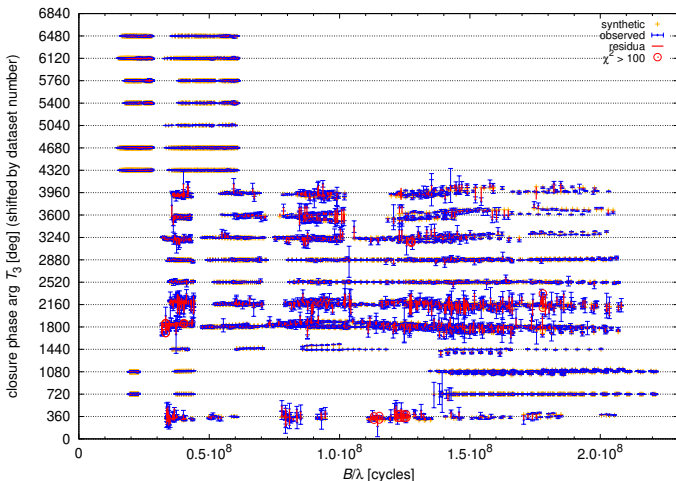


Fig. 9. Similar as Fig. 8, for the closure phase $\arg T_3$ versus B/λ .

solved and thus contribute more to FUV, NUV fluxes. On contrary, χ^2_{sed} increased from 8578 to 9832, due to the same reasons. The most sensitive term seems to be χ^2_{spe} which increased substantially from 588454 to 682016, because $H\alpha$ line profiles are slightly ‘sharper’ and the $\text{He I } 6678$ emission is enhanced; although the profiles remain qualitatively very similar. Other contributions are slightly decreased. This conclusion is preliminary, though, without a repeated convergence. In principle, even the high-resolution model could be converged again which would decrease the increased χ^2 . We conclude the model is resolution dependent. However, this is not necessarily a bad thing; a low-resolution model may simply represent shallower gradients, or not so sharp transitions between objects.

5.2. Distance fixed to 294 pc

First, let us compare our distance with Bastian (2019), who discovered the Gaia 8 cluster, with parallaxes around 3.4 mas or distance 294 pc, and the intrinsic dispersion of only 0.06 mas (i.e., 5 pc radial, 1° spatial). β Lyr A is located in the middle (spa-

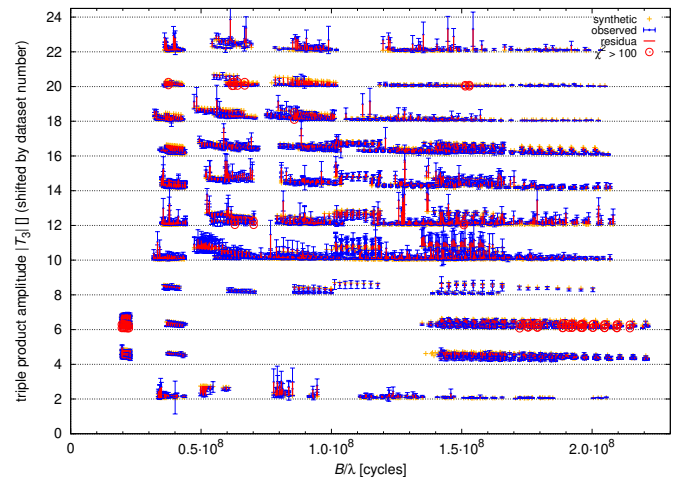


Fig. 10. Similar as Fig. 8, for the triple product $|T_3|$ versus B/λ .

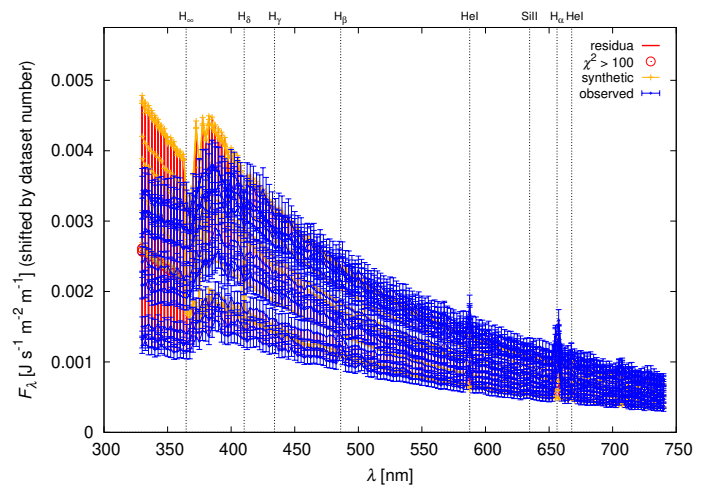


Fig. 11. Spectral-energy distribution (SED) overplotted for 10 phases. Synthetic SEDs systematically differ from observations, especially in NUV and in the vicinity of the Balmer jump. This is not the best model in terms of χ^2_{sed} , but cf. Fig. A.5.

tially); if it is also in the centre of mass, then our photo-spectro-interferometric value $d = (328 \pm 7)$ pc is substantially larger.

If we fix the distance in our model to $d = 294$ pc instead, and converge the model, we obtain different parameters, of course. In particular, in Tab. 4 (column ‘294pc’) we can see that secondary temperature $T_{\text{cp}} = 13512$ K is lower, and disk outer radius $R_{\text{outnb}} = 35.2 R_\odot$ is larger. While the overall fit seems better, $\chi^2_{\text{R}} = 16.9$ (as compared to 17.0), mostly because $\chi^2_{\text{spe}}, \chi^2_{\text{vamp}}$ contributions were improved, it is at the expense of other terms being much worse! Especially χ^2_{sed} was increased three times which is unacceptable for us, and $\chi^2_{\text{vis}}, \chi^2_{\text{clo}}$ were increased too. Moreover, disk outer radius is too large and overshoots not only the tidal cutoff radius $26.3 R_\odot$ (possible in principle as the disk is not an isolated system during ongoing mass transfer), but also its Roche lobe. This is the reason why we still prefer the original model.

5.3. The mass ratio

We cannot make the primary M_\star and secondary mass M_{cp} free when we keep $a \sin i$ and the period P ‘fixed’. Nevertheless, if we free the mass ratio q (and also all other parameters), it affects mainly the size of the donor, which is the major source of

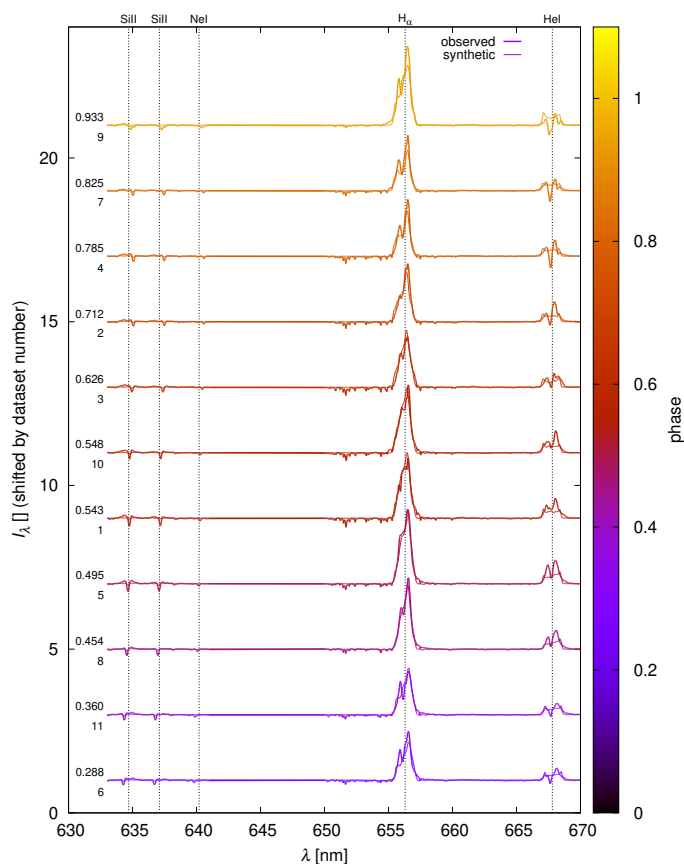


Fig. 12. Normalized spectra $I(\lambda)$ for 11 phases. Both observed (thick) and synthetic (thin) spectra are plotted for comparison. Colours correspond to the phases (see also the values on the left). Uncertainties are not plotted, but they are of the order of 0.01. The vertical lines correspond to (from left to right): Si II 6347, Si II 6371, Ne I 6402, H_α , He I 6678 wavelengths.

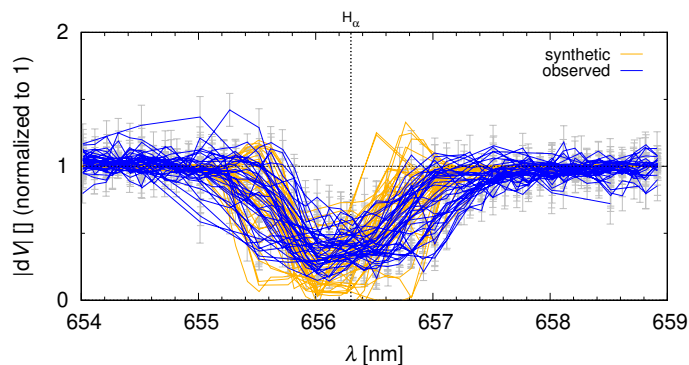


Fig. 13. Differential visibilities $|dV|$ vs λ normalized in continuum. Synthetic (yellow) visibilities for the joint model exhibit a similar decrease across the H_α profile as the observed ones (blue). However, some of the synthetic $|dV|$'s are systematically lower in the blue wing and higher in the red wing.

light. We obtained parameters shown in Tab. 4 (column 'QRA-TIO'). While a majority of them remained close to the previous (local) minimum, the value of $q = 0.2177$ is lower. Because we introduced one more parameter, it is logical that the overall fit is better, with $\chi_R^2 = 16.5$. However, we do not consider the respective changes of parameters to be substantial.

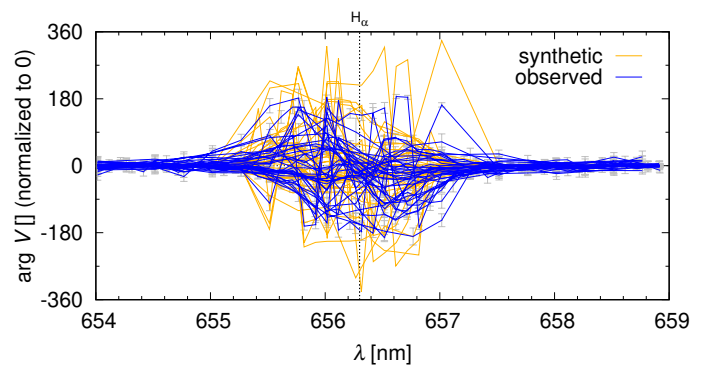


Fig. 14. Similar as Fig. 13, for the differential phases $\arg dV$ versus λ . On average, phase changes are comparable in both observed and synthetic data. There are some remaining phase slips which are also fitted for.

Table 3. Free parameters related to the spot.

parameter	unit	SPOT
R_{sp}	R_\odot	5.28
T_{sp}	K	7146
ρ_{sp}	10^{-9} g/cm^3	9.97
R_{polsp}	R_\odot	29.9
v_{polsp}	km/s	2
α_{sp}	deg	9

Notes. R_{sp} denotes the spot radius, T_{sp} temperature, ρ_{sp} density, R_{polsp} radial offset, v_{polsp} polar velocity, and α_{sp} polar angle. The remaining parameters were included in Tab. 4, column 'SPOT'.

5.4. Spot-like asymmetry

Similarly as in Mourard et al. (2018), we introduced a spot in our model, which represents an additional spherical object. We converged not only spot parameters, but also all other parameters, to be sure that all objects can adapt to new geometrical constraints. The results are listed in Tab. 3 (for the spot itself) as well as in Tab. 4 (column 'SPOT'). We see a minor improvement of the light curve, spectra and differential interferometry, at the expense of other datasets though (the reduced χ_R^2 decreased to 16.8). The position of the spot converged close to the donor-gainer line and the distance corresponds to the outer radius of the disk. Consequently, such a spot may represent either a part of the flow from the donor, the base of the jets, or an asymmetry of the disk rim. We consider the existence of this spot likely, although not so prominent as before (cf. Mourard et al. 2018), because there are additional objects in our model.

5.5. Asymmetric jets

Our stringent geometrical constraints may be partly relaxed by using the parameter a_{symjt} which allows for an asymmetry of the jets (Eq. (19)). The resulting model is shown in Tab. 4, column 'ASYMJT'. As before, we introduced one more parameter and it is not surprising that the fit is better, with $\chi_R^2 = 16.5$. However, the resulting value $a_{\text{symjt}} = 0.02$ is not far from zero. It seems that this additional parameter actually allowed for tiny adjustments of other parameters and we cannot conclude that jets are asymmetric.

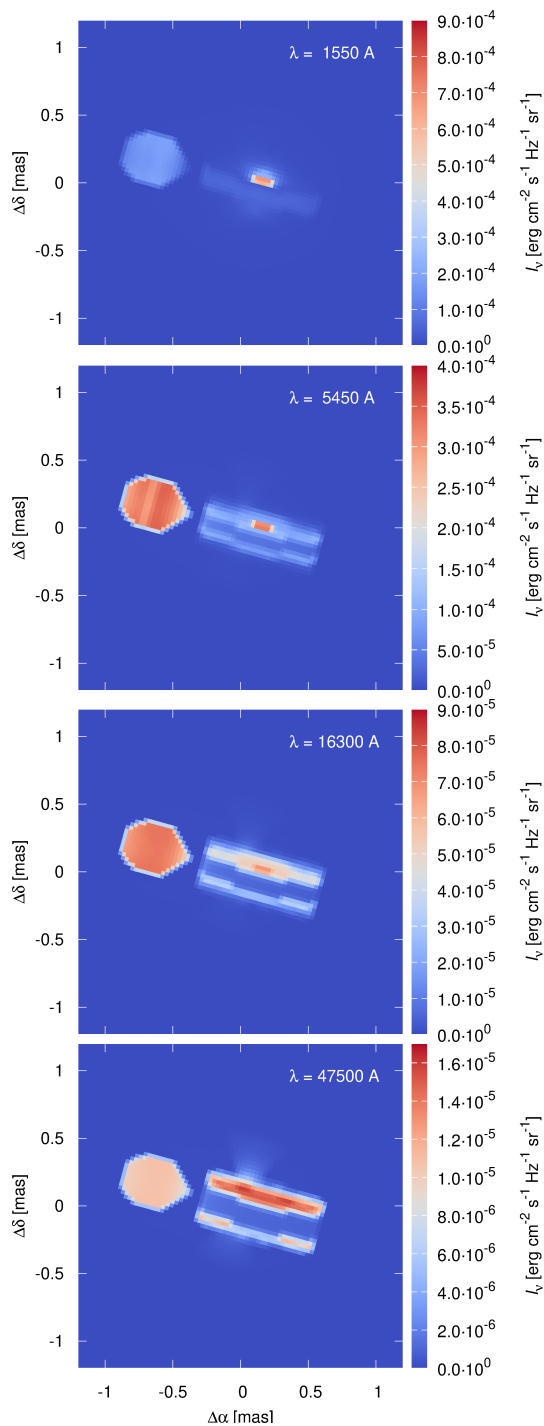


Fig. 15. Continuum synthetic images of β Lyr A for the joint model, computed for four monochromatic wavelengths (from top to bottom): 155 nm (FUV), 545 nm (V), 1630 nm (H), 4750 nm (FIR). The orbital phase is always 0.25. The appearance of the system changes substantially. Optically-thin components (disk atmosphere, jet, shell) are not seen very well in continuum radiation.

5.6. Jet temperature gradients

The fit of the He I 6678 line is far from being perfect. To improve it, we used a model with a substantial temperature gradient $T(r)$ in the jets. We obtained a significantly better fit ($\chi_R^2 = 16.4$; see Tab. 4, column 'ETMPJT') with the slope $e_{\text{tmpjt}} = -0.55$ and the temperature at the base of the jets up to $T_{\text{jt}} \approx 30000$ K. It seems to improve both H α and He I line profiles. Although the

systematics in the core of He I line remained qualitatively the same, there are improvements in the wings of both lines. The parameters of these jets are reasonable because their temperature corresponds very well to the temperature of the gainer and the exponent to the heating by irradiation from the gainer. Consequently, it may be considered as our preferred model.

5.7. Shell temperature gradients

We also tried to enforce the temperature gradient in the shell by initially decreasing the slope $e_{\text{tmpsh}} = -0.5$ and adjusting the temperature $T_{\text{sh}} = 20000$ K accordingly (to end up with 6000 K at R_{outsh}). All parameters were converged again and the result is shown in Tab. 4 (column 'ETMPSH'). We can see the gradient is preserved, but the fit is worse with $\chi_R^2 = 18.1$, especially the χ_{spe}^2 term. The problem is that the gradient affects also all other lines (H α , Si II, Ne I), creates an excess emission which prevents further convergence.

5.8. Low C abundance

We tried to use higher abundances for Si and Ne in order to explain the depth of the respective lines. On the other hand, according to Section 4, there might be 100 times lower abundance of C in surface layers and consequently in the CSM. Our spectra do contain the region of C II 6578 and 6583 lines, but they are too weak. Nevertheless, we checked synthetic spectra with these transitions and solar abundance ($3.31 \cdot 10^{-4}$ by the number of atoms; Grevesse & Sauval 1998). It turned out it would create so strong C II emission, similarly wide as H α , that the abundance must be low (see Figure 20). The abundance 10^{-2} of the solar value is fully compatible with observations; the upper limit is about 10^{-1} . Subsequently, these low abundances were also applied in the 'joint' model.

5.9. He-rich abundance

If we would like to use the non-solar abundances of Balachandran et al. (1986), the situation is much more complicated. We must not use standard atmospheric models, because the abundances $N(\text{H}) = 0.4$, $N(\text{He}) = 0.6$ do change their hydrostatic profiles and the emerging spectra must be different.

As a preliminary check, we computed several NLTE models with the program Tlusty (Hubený & Lanz 1995, 2017). For the modified chemical composition, it was necessary to improve the convergence by adjusting several parameters.³ The output of Tlusty was then used as an input for the program Synspec (Lanz & Hubený 2007; Hubený & Lanz 2017), to obtain a detailed synthetic spectrum; with the line list of Kurucz. We computed spectra only for the effective temperature 14000 K and a limited wavelength range 6330 to 6700 Å (see Figure 21). The level of continuum is by 3 % higher for He-rich abundances. The (non-rotated) H α line profile shows Lorentzian wings deeper by 6 % and He I 6678 line exhibits a significant central absorption. Luckily, after rotational broadening, the profiles will not be so different from standard ones and we proceed without an extensive computation of a new grid of synthetic spectra. Moreover, one of our stars (primary, gainer) is partly hidden within the disk and its radiation is reprocessed by circumstellar matter.

For simplicity, we thus use He-rich abundances only for the CSM. The result is shown in Tab. 4 (column 'H0.4_He0.6'). The

³ namely ND = 70, NITER = 50, ITEK = 20, TAUDIV = 1.0

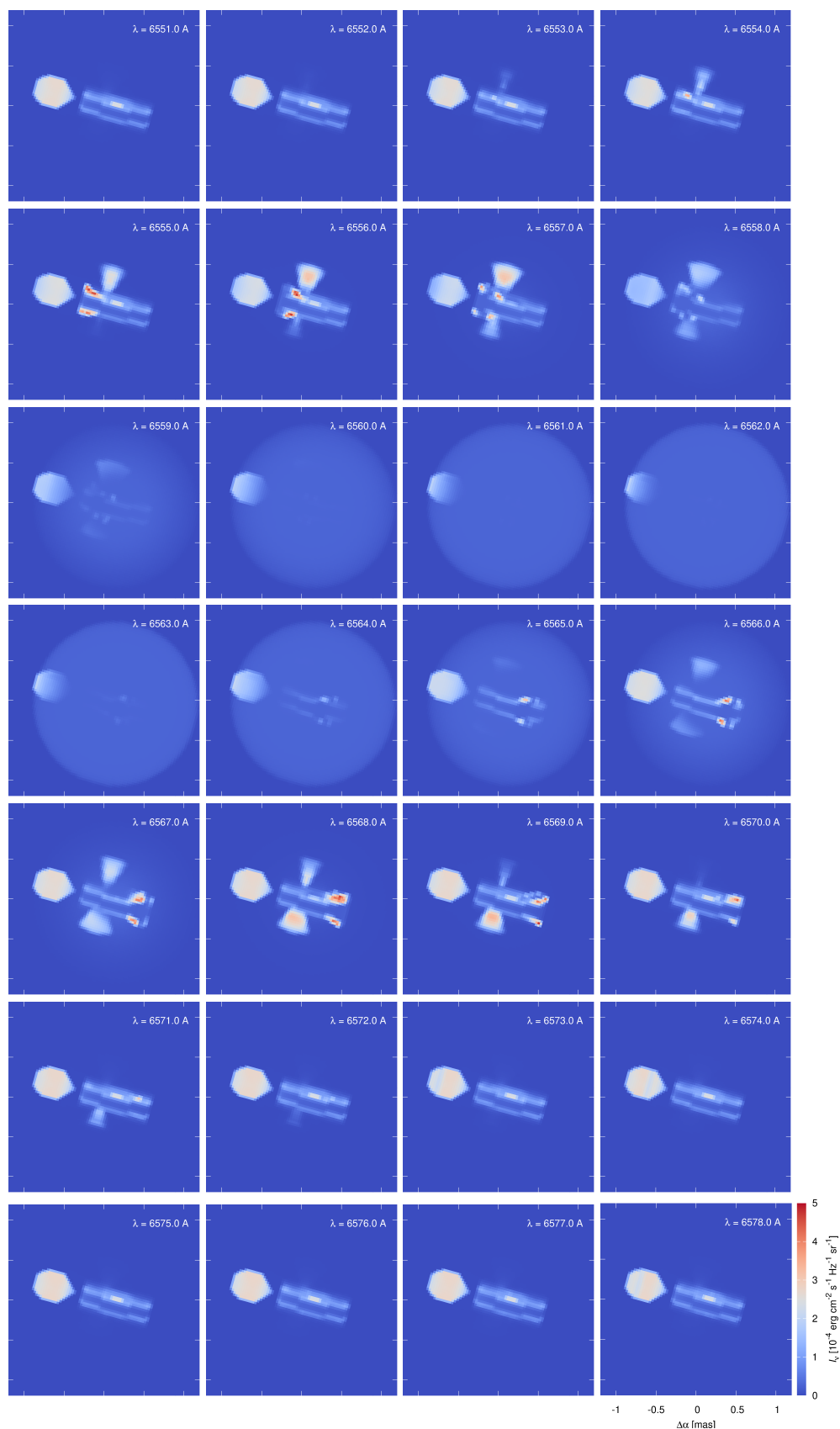


Fig. 16. Line-profile synthetic images of β Lyr A computed for the wavelength range of $H\alpha$, i.e., from 655.1 to 657.8 nm, at a *fixed* phase 0.25. Optically-thin components are clearly visible. The disk atmosphere appears first, because its Keplerian velocities close to the inner rim produce the blue-shifted wing. The jet inclined towards the observer appears second, with high velocities being projected to the line of sight. Finally, there is the spherical shell, with relatively low velocities spanning the core of $H\alpha$, which obscures other small-scale structures. For $\lambda > 6563$ Å, all objects disappear in a reverse order. An animated version is available at <https://sirrah.troja.mff.cuni.cz/~mira/betalyr/>.

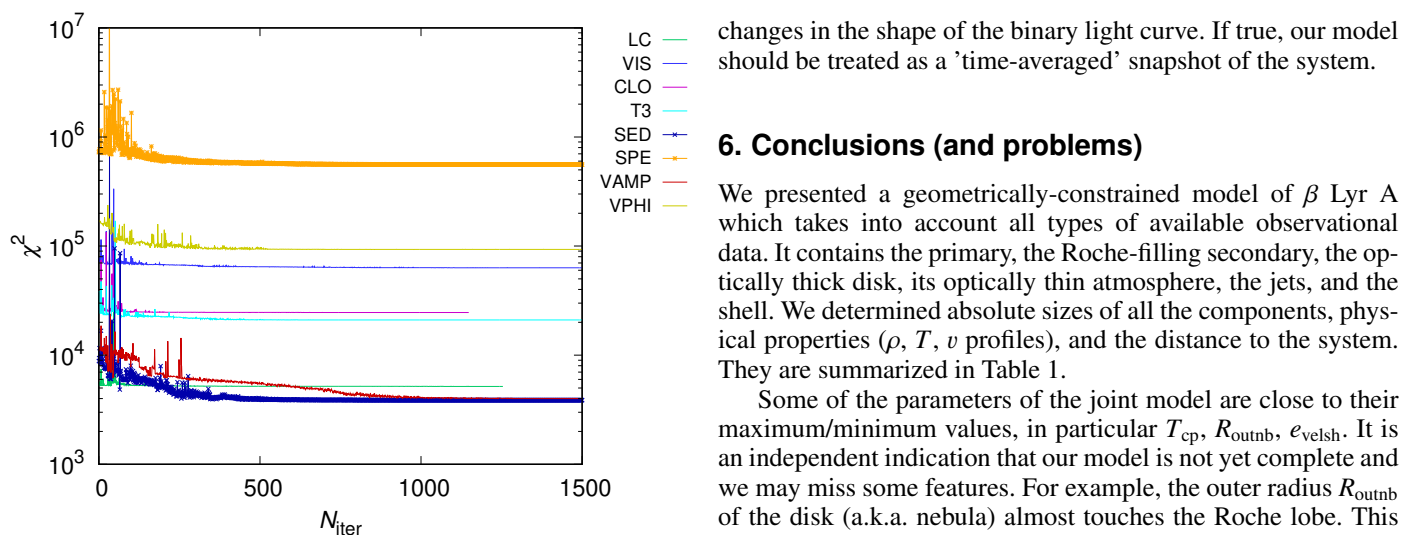


Fig. 17. The χ^2 convergence for observation-specific models, when starting from the best-fit joint model. After performing up to 10^3 iterations, substantial improvements were achieved for some datasets (LC, T3, SED, VAMP, ...). It confirms systematic differences between observational datasets.

model does converge, but the overall $\chi_R^2 = 19.5$ remained high, with χ_{spe}^2 being the dominant term. On the basis of our modelling we thus cannot confirm that abundances are He-rich.

5.10. Differential visibility in He I 6678

There are additional interferometric datasets, namely differential visibilities in He I 6678 line. We performed a comparison only, not convergence. According to Figure 22 and Figure 23, there are systematic differences, with synthetic $|dV|$'s being often flatter than observed $|dV|$'s. The problem is likely the same as in Section 5.7, i.e., unidentified temperature gradients which would create extended hot emission regions of He I (but not of H α). The comparison of these two figures with the similar ones for H α (Figure 13 and Figure 14) is however very instructive. It is easily seen that the He I data are firstly less resolved in the core of the line than in H α and secondly that almost no phase signal is detected. This result is in favor of a behavior dominated by the shell structure without any role for the jets here.

5.11. Additional high-resolution spectroscopy

There are also additional spectroscopic datasets, particularly the one obtained at the Ritter Observatory and used by Ignace et al. (2018). It has a higher resolution than our spectra ($\lambda/\Delta\lambda = 26000$) and a very good phase coverage. The spectra were acquired in different seasons (1996 to 2000). When we performed a comparison, not convergence, of 11 representative spectra there were systematic differences, mainly in the observed emission peak around the primary eclipse (i.e., the donor eclipsed, not the gainer) which is substantially higher than in our model. The observed H α profiles also do contain smaller features which are not reproduced by our model. Nevertheless, the model can easily be adapted to the overall emission (e.g., by adjusting densities ρ_{nb} , ρ_{jt} , ρ_{sh} , or by moving the jet along with $\alpha_{\text{jt}} \simeq -140^\circ$ where a 2nd local minimum of χ_{spe}^2 is located). It may be an indication that the distribution of optically-thin CSM had been evolving on the time scale of >10 years (or >300 orbits). Several investigators, most recently Rucinski et al. (2019), noted also cycle-to-cycle

changes in the shape of the binary light curve. If true, our model should be treated as a 'time-averaged' snapshot of the system.

6. Conclusions (and problems)

We presented a geometrically-constrained model of β Lyr A which takes into account all types of available observational data. It contains the primary, the Roche-filling secondary, the optically thick disk, its optically thin atmosphere, the jets, and the shell. We determined absolute sizes of all the components, physical properties (ρ , T , v profiles), and the distance to the system. They are summarized in Table 1.

Some of the parameters of the joint model are close to their maximum/minimum values, in particular T_{cp} , R_{outnb} , e_{velsh} . It is an independent indication that our model is not yet complete and we may miss some features. For example, the outer radius R_{outnb} of the disk (a.k.a. nebula) almost touches the Roche lobe. This may induce perturbations and a precession of the disk. These instabilities are not accounted for in our model. Additionally, the outer rim may not be in an exact equilibrium, because of the ongoing mass transfer, and the secondary may induce spiral arms, i.e., azimuthal variations in the disk (Panoglou et al. 2019).

The mass loss rate from jets is substantial. Given the surface area at the beginning of the cone, $S = 2\pi R_{\text{injt}}^2(1 - \cos \alpha_{\text{jet}})$, and the respective expansion velocity, we get $\dot{M}_{\text{jt}} = 2S v_r \rho_{\text{jt}} \simeq 8.3 \cdot 10^{-7} M_\odot \text{yr}^{-1}$ which is about 4% of the mass transfer rate $\dot{M} \simeq 2 \cdot 10^{-5} M_\odot \text{yr}^{-1}$. Consequently, the mass transfer is not conservative, but it is not far from being conservative. The time scale related to the jets is $\tau \simeq R_{\text{outjt}}/v_{\text{jt}} \simeq 0.5$ d which is shorter than the orbital period. The jets are continuously replenished as they follow the orbital motion. It is interesting to integrate the mass loss over long time scales and check observationally where the (expanded and cooled-down) CSM is located. According to Umana et al. (2000) measurements of the radio emission, the CSM is very extended ($145 \text{ mas} \hat{=} 10^4 R_\odot$ at our d) and the integrated mass is $M \simeq 0.015 M_\odot$. Consequently, the time scale would be of the order of $\tau \simeq M/\dot{M}_{\text{jt}} \simeq 10^5$ yr which agrees with the binary evolution time scale (van Rensbergen & De Greve 2016).

We kept masses of both components more-or-less fixed, in accord with previous spectroscopic analyses of individual absorption lines (Si II, Ne I). The distance is then determined mainly from interferometry and the SED, but spectroscopy (SPE) is also affected, because Keplerian velocity fields are determined by central masses. Let us recall that our preferred distance $d = (328 \pm 7) \text{ pc}$ is larger than 294 pc inferred by Bastian (2019) (see Section 5.2).

Looking at synthetic profiles of the He I 6678 line in detail, it is in a broad emission (due to the inner hot edge of the disk and Keplerian broadening), but the observed profile is steeper, double-peaked, with a red peak being stronger and a blue-shifted central absorption (i.e., very similar to H α). Consequently, the inner edge should be even more visible and should exhibit some absorption due to winds. Our model cannot easily adapt to this, because the emission in H α would be increased immediately and we already match its EW. Moreover, the differences in the H α and He I are of the same order, which is an indication of a compromise.

On contrary, the synthetic Si II 6347 and 6371 lines tend to produce a broad emission and a weak absorption, even at an increased metallicity, but the observed Si II's exhibit deeper absorptions. Similarly, the synthetic Ne I 6402 line is in a broad (disk) emission, but observed profile is rather flat.

Table 4. Free parameters, fixed parameters, χ^2 values for a joint model and for several alternative models.

parameter	unit	joint	294pc	QRATIO	SPOT	ASYMJT	ETMPJT	ETMPSH	H0.4_He0.6
T_{cp}	K	14334	13512	14525	14580	14566	14085	14580	14293
R_{innb}	R_{\odot}	8.7	8.2	8.8	8.7	8.7	10.2	9.5	10.4
R_{outnb}	R_{\odot}	31.5	35.2	31.0	30.3	31.2	30.3	32.8	31.0
h_{inbnb}	H	3.5	4.4	3.6	3.5	3.8	4.4	3.9	3.7
T_{inbnb}	1	1.5	1.8	1.5	1.5	1.5	1.5	1.5	1.8
h_{windnb}	H	3.0	4.0	3.0	3.0	3.0	3.0	3.1	3.1
h_{cnb}	H	3.8	3.1	3.6	3.7	3.6	3.8	2.9	2.9
v_{nb}	km/s	112	106	111	114	107	123	102	120
e_{velnb}	1	1.91	1.57	1.95	1.91	1.96	1.69	1.94	1.99
h_{shdnb}	H	5.0	5.0	4.8	3.9	4.8	5.0	4.3	4.9
T_{nb}	K	30345	30558	30443	30435	30836	29398	31233	32619
ϱ_{nb}	10^{-9} g/cm ³	1.21	4.86	1.21	1.25	1.20	0.91	1.62	1.15
v_{trbnb}	km/s	11	99	13	12	12	25	12	16
e_{denbn}	1	-0.57	-0.55	-0.56	-0.57	-0.54	-0.57	-0.59	-0.59
e_{tmpnb}	1	-0.73	-0.70	-0.73	-0.73	-0.73	-0.73	-0.73	-0.71
a_{jet}	deg	28.8	32.7	28.8	28.7	28.9	28.8	21.4	32.0
R_{injt}	R_{\odot}	5.6	6.6	5.6	5.6	5.6	5.4	5.8	5.5
R_{outjt}	R_{\odot}	35.9	34.3	35.9	36.0	36.0	37.3	35.0	40.3
v_{jt}	km/s	676	535	679	671	674	661	880	627
T_{jt}	K	15089	22702	15150	15440	14668	30014	15822	13902
ϱ_{jt}	10^{-12} g/cm ³	5.52	6.74	5.48	5.53	5.47	5.11	7.97	5.55
v_{trbjt}	km/s	66	31	60	65	61	61	97	69
R_{poljt}	R_{\odot}	33.0	3.6	32.4	33.1	32.5	33.0	33.3	34.0
v_{poljt}	km/s	10	3	11	10	14	14	28	17
α_{jt}	deg	-70	-28	-70	-70	-70	-70	-55	-104
R_{insh}	R_{\odot}	7.4	7.3	7.4	7.4	7.4	7.4	7.1	11.1
R_{outsh}	R_{\odot}	72.9	77.0	72.7	73.1	72.8	71.1	69.4	75.7
v_{sh}	km/s	79	98	79	80	78	70	90	87
e_{velsh}	1	1.90	1.97	1.95	1.93	1.96	1.99	1.89	1.93
v_{ysh}	km/s	-5	-37	-3	-3	-4	-5	10	-23
T_{sh}	K	5631	5549	5628	5620	5637	5631	18888	5678
ϱ_{sh}	10^{-11} g/cm ³	2.86	1.42	2.92	2.94	2.91	2.86	0.90	3.05
v_{trbsh}	km/s	102	134	101	102	99	95	96	96
I	deg	96.3	96.2	96.3	96.3	96.3	96.4	96.9	96.4
Ω	deg	254.6	254.9	254.6	254.6	254.6	254.0	255.0	254.6
d	pc	328.4	294.0	328.6	328.5	328.6	325.7	329.5	328.6
M_{\star}	M_{\odot}	13.048	13.048	13.260	13.048	13.048	13.048	13.048	13.048
q	1	0.2230	0.2230	0.2177	0.2230	0.2230	0.2230	0.2230	0.2230
a_{symjt}	1	0.00	0.00	0.00	0.00	0.02	0.00	0.00	0.00
e_{veljt}	1	1.27	1.29	1.24	1.29	1.21	1.39	1.67	1.25
e_{tmpjt}	1	0.00	0.00	0.00	0.00	0.00	-0.55	0.00	0.00
e_{tmpsh}	1	-0.01	-0.01	-0.01	-0.01	-0.01	-0.00	-0.64	-0.00
N_{iter}	–	2761	965	946	228	1300	1721	1615	879
N	–	45102	45102	45102	45102	45102	45102	45102	45102
χ^2	–	767681	763215	743809	755684	743503	739977	818502	878773
χ^2_{R}	–	17.0	16.9	16.5	16.8	16.5	16.4	18.1	19.5
χ^2_{lc}	–	7083	11545	6937	6707	6964	6954	8489	8323
χ^2_{vis}	–	56941	77843	57526	57771	57837	56017	56773	69041
χ^2_{clo}	–	25910	41057	25632	25792	25598	25786	27332	27355
χ^2_{I3}	–	16194	11845	17183	18141	17455	14690	16291	24981
χ^2_{sed}	–	8578	24490	8989	10018	9289	10035	14463	13188
χ^2_{spe}	–	588455	537458	565051	573972	564484	565680	640013	671153
χ^2_{vamp}	–	5959	4478	5951	5884	6017	5833	6958	5016
χ^2_{vphi}	–	58562	54498	56541	57398	55859	54982	48183	59716

Notes. The quantities are the same as in Tab. 1. The model with jet temperature gradients (denoted 'ETMPJT') is our preferred model, as explained in Section 5.6.

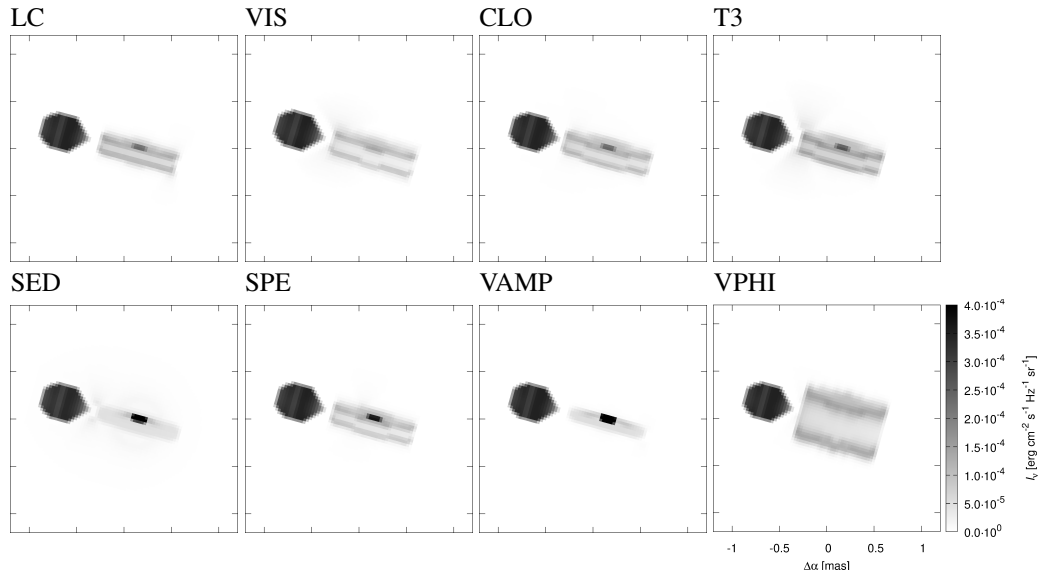


Fig. 18. Continuum synthetic images for observation-specific models (datasets LC, VIS, CLO, T3, SED, SPE, VAMP, VPHI) for the wavelength 545 nm (V). The apparent differences (e.g., the thickness of the disk, the appearance of the primary) demonstrate systematics between datasets. Alternately, some datasets (e.g., VPHI) do not constrain certain parameters.

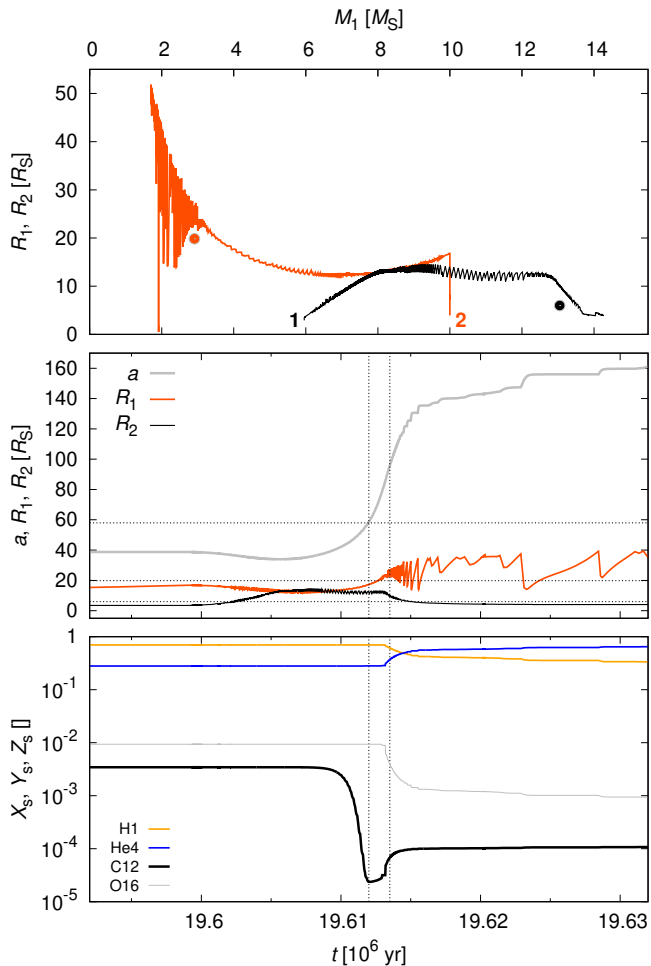


Fig. 19. Stellar evolution of a binary corresponding to β Lyr A. The component radii R_1 , R_2 vs the primary mass M_1 are plotted (top), with observed values indicated by full circles, together with the distance a and R_1 , R_2 vs time t (middle), cf. horizontal dashed lines, and surface abundances X , Y , A_{C12} , A_{O16} vs time t (bottom). At $t = 19.613 \cdot 10^6$ yr, the mass ratio q corresponds to the observed one.

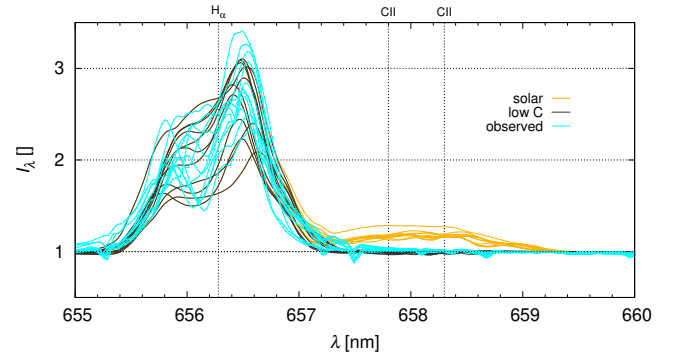


Fig. 20. Synthetic spectra for the solar abundances (yellow) and 10^{-2} lower abundance of C (gray); observed spectra (blue) are plotted for comparison. For the solar composition, C II 6578 and 6583 emission is too strong.

According to a standard stellar evolution, the metallicity of the stellar surfaces – as well as of the CSM – can be substantially different from normal (solar), if the mass transfer has reached chemically modified layers. For the parameters corresponding to our model, we expect a low abundance of C (by a factor of 10^2). A likely final outcome would be a detached system with a He-rich dwarf (similar to ϕ Per; Mourard et al. 2015).

From the technical point of view, our model is somewhat resolution-dependent. The peak densities or temperatures are not necessarily well resolved; in other words, the profiles are effectively shallower/smoother. A higher resolution may be also needed to obtain smooth P Cygni profiles in thin layers with velocity gradients, such as in expanding atmospheres.

In order to improve the convergence of our model, it may be useful to use the least correlated parameters. For example, the total mass of the shell (instead of R_{insh} , R_{outsh} , and ρ_{sh}), or a suitable reference radius (between R_{innb} , R_{outnb} ; inclusive), in accord with observational datasets, which are sensitive either to outer, or inner radii; in our case, outer seems better.

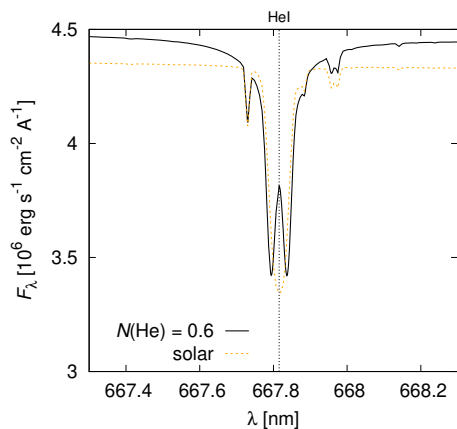


Fig. 21. Non-rotated NLTE synthetic spectra computed for stellar atmospheres with He-rich ($N(\text{H}) = 0.4$, $N(\text{He}) = 0.6$; black) and solar (orange) compositions. The effective temperature was 14000 K in both cases. For the He-rich case, the profile exhibits a central absorption.

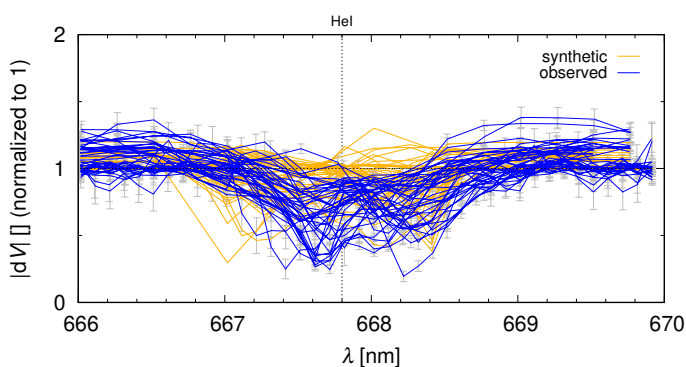


Fig. 22. Differential visibility amplitude $|dV|$ for the He I 6678 line. The joint model was used, but no convergence of the respective He I VAMP dataset.

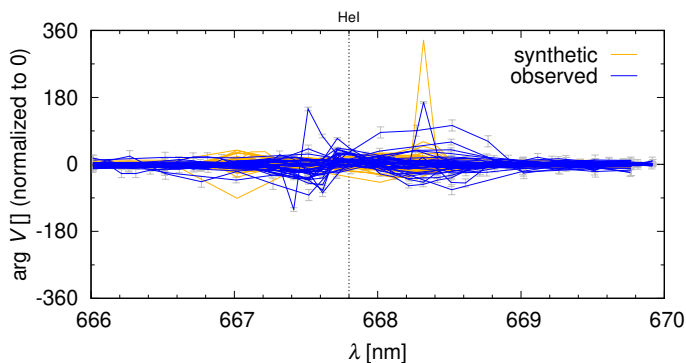


Fig. 23. Differential visibility phase $\arg dV$ for the He I line. Again, the joint model, but no convergence.

Nevertheless, in spite of the remaining limitations discussed above, it is encouraging that our modelling of an extended set of different types of observational data led to a generally consistent *quantitative* picture of the system. We note that the principal physical properties obtained from several specific considered models are numerically quite stable, not too different from one model to another. Our models nicely confirm the conjecture that the so called B spectrum (introduced and discussed in the classical early studies of β Lyr A) originates mainly in the jets, the disk atmosphere or other circumstellar matter above/below the orbital plane, including their blueshift of about 50 to 100 km s⁻¹

(Harmanec 1992; Harmanec et al. 1996; Bonneau et al. 2011). Also the presence of an extended shell, observationally detected by Ak et al. (2007), is required by our model and data. Another important result of this study is a convincing confirmation of the strong carbon underabundance, in accord with the models of the large-scale mass exchange in binaries. We thus believe that the present study constitutes a good starting point to even more sophisticated modelling of the system.

Acknowledgements. We thank J.A. Nemravová for the initial development of the PysHELLSPEC. We also thank P. Koubský, R. Kříček, D. Korčáková as well as J.A.N., who obtained some of the spectra used in this study. We thank R. Ignace for providing us with his reduced spectra from the Ritter Observatory in phase space and for illuminating comments on his study. We also acknowledge the Ritter Observatory for making the archive of spectra public. M.B. and P.H. were supported by the Czech Science Foundation grant 19-01995S. J.B. was supported by the VEGA 2/0031/18 grant and by the Slovak Research and Development Agency under the contract No. APVV-15-0458. H.B. acknowledges financial support from the Croatian Science Foundation under the project 6212 “Solar and Stellar Variability”. The CHARA Array is supported by the National Science Foundation under Grant No. AST-1636624 and AST-1715788.

References

- Ak, H., Chadima, P., Harmanec, P., et al. 2007, *A&A*, 463, 233
 Armstrong, J. T., Mozurkewich, D., Rickard, L. J., et al. 1998, *ApJ*, 496, 550
 Atwood-Stone, C., Miller, B. P., Richards, M. T., Budaj, J., & Peters, G. J. 2012, *ApJ*, 760, 134
 Balachandran, S., Lambert, D. L., Tomkin, J., & Parthasarathy, M. 1986, *MNRAS*, 219, 479
 Bastian, U. 2019, *A&A*, 630, L8
 Bonneau, D., Chesneau, O., Mourard, D., et al. 2011, *A&A*, 532, A148
 Budaj, J. 2011, *AJ*, 141, 59
 Budaj, J. & Richards, M. T. 2004, *Contributions of the Astronomical Observatory Skalnaté Pleso*, 34, 167
 Budaj, J., Richards, M. T., & Miller, B. 2005, *ApJ*, 623, 411
 Burnashev, V. I. & Skulskii, M. Y. 1978, *Bull. Crimean Astrophys. Obs.*, 58, 53
 Green, G. M., Schlafly, E. F., Finkbeiner, D. P., et al. 2015, *ApJ*, 810, 25
 Grevesse, N. & Sauval, A. J. 1998, *Space Sci. Rev.*, 85, 161
 Harmanec, P. 1992, *A&A*, 266, 307
 Harmanec, P. 2002, *AN*, 323, 87
 Harmanec, P., Morand, F., Bonneau, D., et al. 1996, *A&A*, 312, 879
 Heber, U. 2009, *ARA&A*, 47, 211
 Horn, J., Kubát, J., Harmanec, P., et al. 1996, *A&A*, 309, 521
 Hubený, I. & Lanz, T. 1995, *ApJ*, 439, 875
 Hubený, I. & Lanz, T. 2017, *arXiv e-prints*, arXiv:1706.01859
 Husser, T.-O., Wende-von Berg, S., Dreizler, S., et al. 2013, *A&A*, 553, A6
 Ignace, R., Gray, S. K., Magno, M. A., Henson, G. D., & Massa, D. 2018, *AJ*, 156, 97
 Krpata, J. 2008, <http://astro.troja.mff.cuni.cz/ftp/hec/SPEFO/>
 Lanz, T. & Hubený, I. 2003, *ApJS*, 146, 417
 Lanz, T. & Hubený, I. 2007, *ApJS*, 169, 83
 Lei, Z., Zhao, J., Németh, P., & Zhao, G. 2018, *ApJ*, 868, 70
 Monnier, J. D., Berger, J.-P., Millan-Gabet, R., & ten Brummelaar, T. A. 2004, in *New Frontiers in Stellar Interferometry*, ed. W. A. Traub, Vol. 5491, 1370
 Mourard, D., Bériou, P., Perraut, K., et al. 2011, *A&A*, 531, A110
 Mourard, D., Brož, M., Nemravová, J. A., et al. 2018, *A&A*, 618, A112
 Mourard, D., Clausse, J. M., Marcotto, A., et al. 2009, *A&A*, 508, 1073
 Mourard, D., Monnier, J. D., Meilland, A., et al. 2015, *A&A*, 577, A51
 Nemravová, J. A., Harmanec, P., Brož, M., et al. 2016, *A&A*, 594, A55
 Panoglou, D., Borges Fernandes, M., Baade, D., et al. 2019, *MNRAS*, 486, 5139
 Paxton, B., Bildsten, L., Dotter, A., et al. 2011, *ApJS*, 192, 3
 Paxton, B., Marchant, P., Schwab, J., et al. 2015, *ApJS*, 220, 15
 Pringle, J. E. 1981, *ARA&A*, 19, 137
 Rowan, N. 1990, Ph.D. thesis, Univ. Texas Austin
 Rucinski, S. M., Pigulski, A., Kuschnig, R., et al. 2019, *AJ*, 158, 148
 Sahade, J. 1966, *Transactions of the International Astronomical Union, Series B*, 12, 494
 Schlafly, E. F. & Finkbeiner, D. P. 2011, *ApJ*, 737, 103
 Skulskii, M. Y. 2020, *arXiv e-prints*, arXiv:2005.10802
 ten Brummelaar, T. A., McAlister, H. A., Ridgway, S. T., et al. 2005, *ApJ*, 628, 453
 Tereshchenko, V. M. & Kharitonov, A. V. 1972, *Trudy Astrofizicheskogo Instituta Alma-Ata*, 21
 Umana, G., Mated, P. F. L., Trigilio, C., et al. 2000, *A&A*, 358, 229
 van Hamme, W. 1993, *AJ*, 106, 2096
 van Rensbergen, W. & De Greve, J. P. 2016, *A&A*, 592, A151

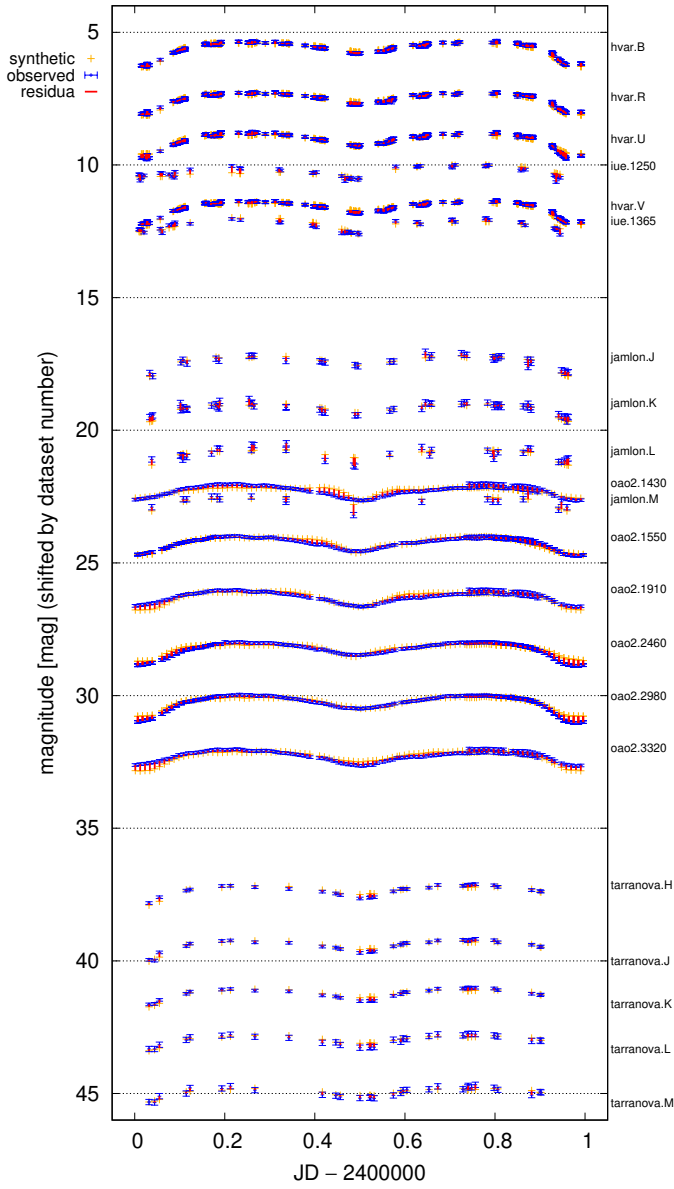


Fig. A.1. The same as Fig. 7 for the observation-specific model.

Appendix A: Figures for observation-specific models

The observation-specific models converged for a given dataset (LC, VIS, CLO, T3, SED, SPE, VAMP, VPHI) are presented in Figures A.1 to A.8. Generally, the individual χ^2 contributions are smaller than for the joint model (see Tab. 1). We take these results also as a confirmation that our model converges and is capable to optimally fit these datasets.

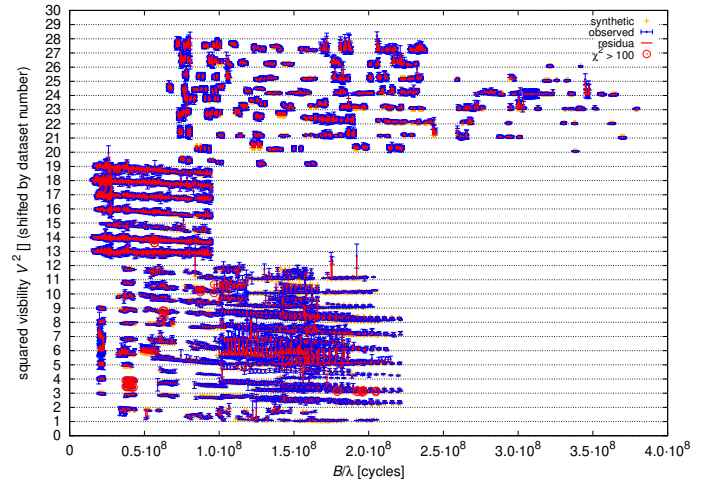


Fig. A.2. The same as Fig. 8 for the observation-specific model.

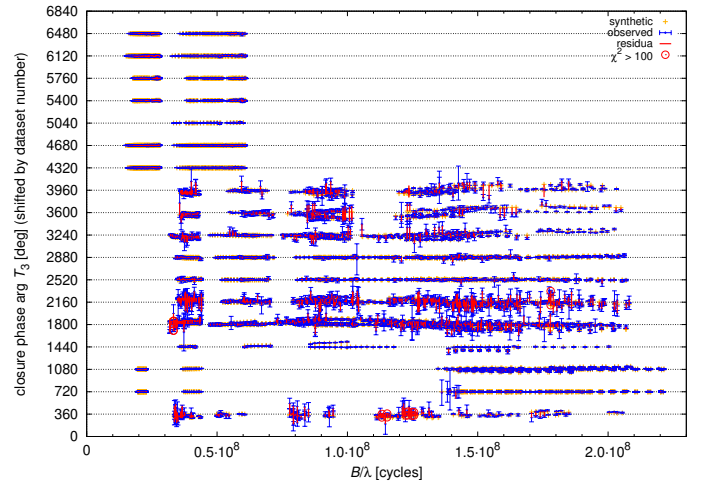


Fig. A.3. The same as Fig. 9 for the observation-specific model.

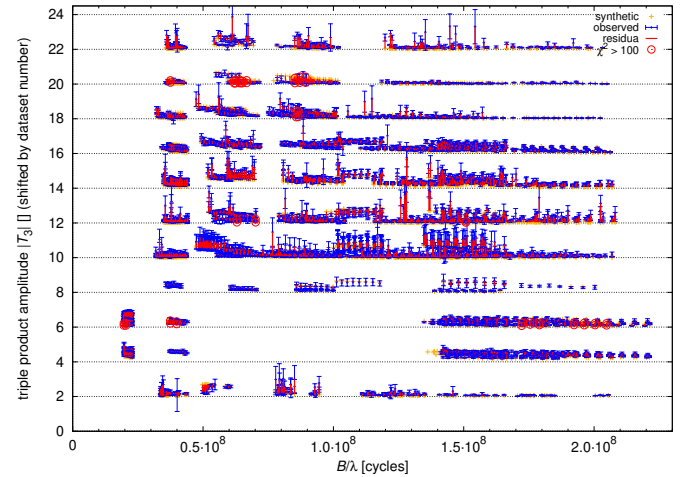


Fig. A.4. The same as Fig. 10 for the observation-specific model.

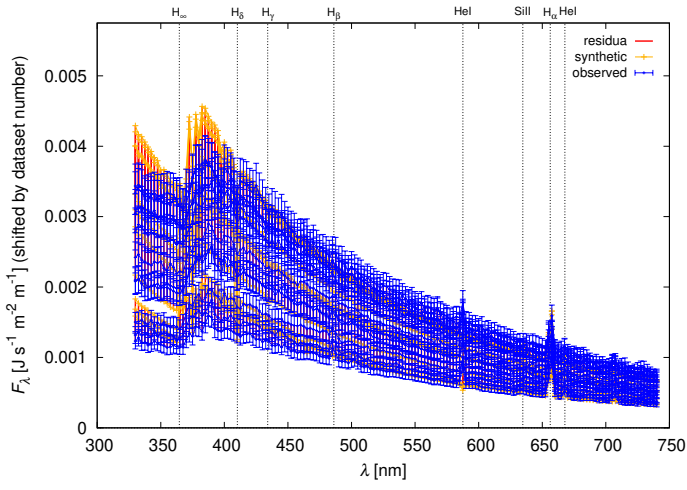


Fig. A.5. The same as Fig. 11 for the observation-specific model.

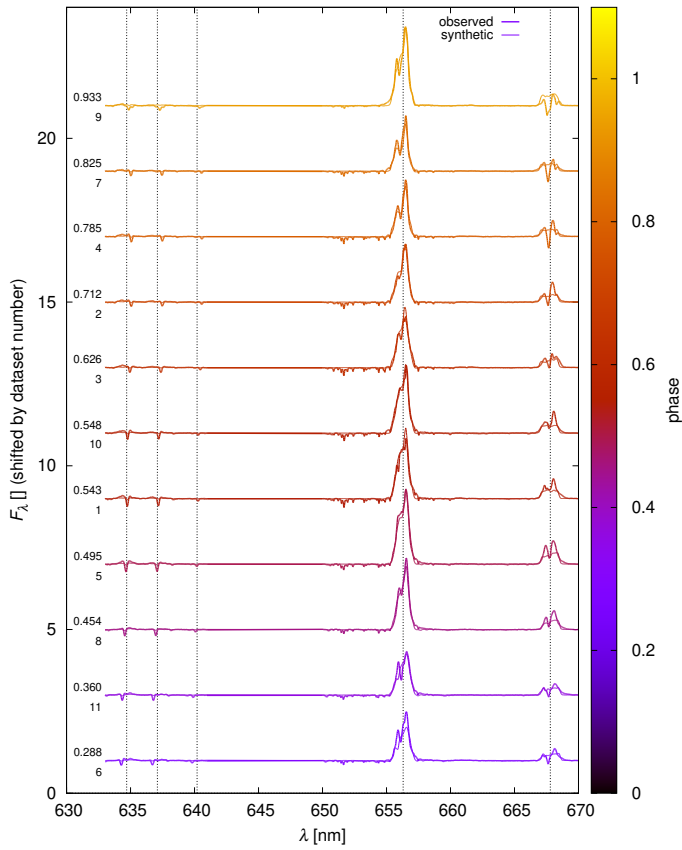


Fig. A.6. The same as Fig. 12 for the observation-specific model.

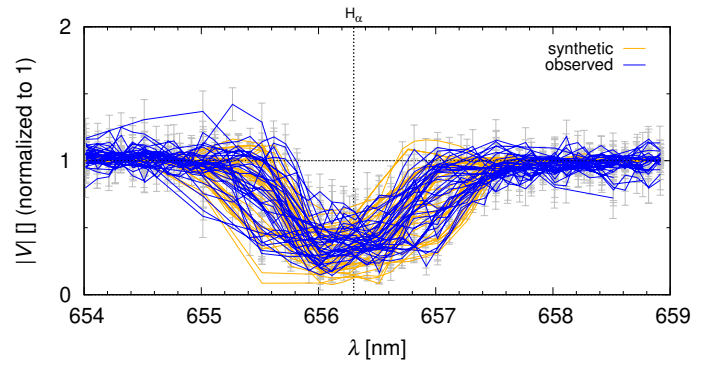


Fig. A.7. The same as Fig. 13 for the observation-specific model.

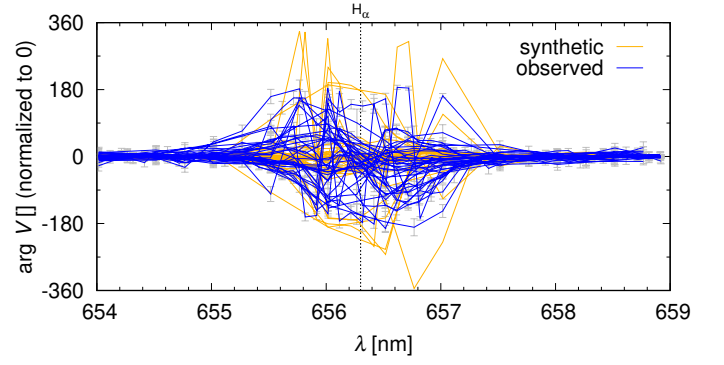


Fig. A.8. The same as Fig. 14 for the observation-specific model.